

REPORT DOCUMENTATION PAGE				Form Approved OMB No. 0704-0188		
The public reporting burden for this collection of information is estimated to average 1 hour per response, including the time for reviewing instructions, searching existing data sources, gathering and maintaining the data needed, and completing and reviewing the collection of information. Send comments regarding this burden estimate or any other aspect of this collection of information, including suggestions for reducing the burden, to the Department of Defense, Executive Service Directorate (0704-0188). Respondents should be aware that notwithstanding any other provision of law, no person shall be subject to any penalty for failing to comply with a collection of information if it does not display a currently valid OMB control number.						
<b>PLEASE DO NOT RETURN YOUR FORM TO THE ABOVE ORGANIZATION.</b>						
1. REPORT DATE (DD-MM-YYYY) 06/28/2011		2. REPORT TYPE Final Report		3. DATES COVERED (From - To) 03/15/2008-04/30/2011		
4. TITLE AND SUBTITLE Tunable Thermal Radiative Properties of Nanotube and Nanowire Arrays				5a. CONTRACT NUMBER FA9550-08-1-0126		
				5b. GRANT NUMBER		
				5c. PROGRAM ELEMENT NUMBER		
				5d. PROJECT NUMBER		
6. AUTHOR(S) Xiulin Ruan Timothy Fisher				5e. TASK NUMBER		
				5f. WORK UNIT NUMBER		
7. PERFORMING ORGANIZATION NAME(S) AND ADDRESS(ES) Purdue University 585 Purdue Mall, West Lafayette, IN 47906				8. PERFORMING ORGANIZATION REPORT NUMBER		
9. SPONSORING/MONITORING AGENCY NAME(S) AND ADDRESS(ES) AFOSR 875 North Randolph St Room 3112 Arlington, VA 22203				10. SPONSOR/MONITOR'S ACRONYM(S)		
				11. SPONSOR/MONITOR'S REPORT NUMBER(S) AFRL-OSR-VA-TR-2012-0235		
12. DISTRIBUTION/AVAILABILITY STATEMENT Distribution A - Approved for Public Releases						
13. SUPPLEMENTARY NOTES						
14. ABSTRACT A multiscale multiphysics simulation tool, by integrating excited state ab initio calculations and FDTD simulations, has been developed. It has the capability of predicting thermal radiative properties of nanotube/nanowire arrays given their atomic structures without using adjustable parameters. Benchmark work is first performed on semiconductor GaAs to demonstrate the effectiveness of our approach. Ab initio calculations on single walled carbon nanotubes (SWCNT) show that the dielectric function is very sensitive to chirality, polarization, and intertube coupling. GW and BSE methods have been successfully used to account for quasi-particle and exciton effects. The dielectric function is used in finite difference time domain (FDTD) simulations to calculate the macroscopic radiative properties of nanotube(NT)/nanowire(NW) arrays. In particular, it is proposed that the optical absorption can be enhanced by using disordered vertical CNT and Si NW arrays. E-beam lithography and atomic layer deposition have been used to synthesize patterned carbon nanotube arrays. Thermal reflectance has been characterized on NT/NW samples, and tunable thermal radiative properties in total reflectance and spectra have been observed.						
15. SUBJECT TERMS						
16. SECURITY CLASSIFICATION OF:			17. LIMITATION OF ABSTRACT	18. NUMBER OF PAGES	19a. NAME OF RESPONSIBLE PERSON	
a. REPORT	b. ABSTRACT	c. THIS PAGE		33	Xiulin Ruan	
					19b. TELEPHONE NUMBER (Include area code) 765-494-5721	

Reset

**Final Report for Grant FA9550-08-1-0126**  
**Period: 03/15/2008-04/30/2011**

## **Tunable Thermal Radiative Properties of Nanotube and Nanowire Arrays**

Xiulin Ruan and Timothy Fisher  
School of Mechanical Engineering and Birck Nanotechnology Center, Purdue University

### ***Abstract***

A multiscale multiphysics simulation tool, by integrating excited state ab initio calculations and FDTD simulations, has been developed. It has the capability of predicting thermal radiative properties of nanotube/nanowire arrays given their atomic structures. Benchmark work is first performed on semiconductor GaAs to demonstrate the effectiveness of our approach, showing that both infrared and visible band radiative properties agree well with experimental data. Ab initio calculations on single walled carbon nanotubes (SWCNT) show that the dielectric function is very sensitive to chirality, polarization, and intertube coupling. GW and BSE methods have been successfully used to account for quasi-particle and exciton effects. The dielectric function is used in finite difference time domain (FDTD) simulations to calculate the macroscopic radiative properties of nanotube(NT)/nanowire(NW) arrays. The results show that the conventional Maxwell-Garnett method is not accurate. The effects of array filling fraction, diameter, and length are investigated systematically. In particular, it is proposed that the optical absorption can be enhanced by using disordered vertical CNT and Si NW arrays. E-beam lithography has been used to synthesize patterned carbon nanotube arrays to achieve good periodicity. Processing of controlled variation (ALD, etching) has been achieved. Thermal reflectance has been characterized on NT/NW samples, and tunable thermal radiative properties in total reflectance and spectra have been observed. The conclusion of this project represents a major advance of multiscale multiphysics understanding of thermal radiative properties of nanotube/nanowire arrays that are of significant technical importance.

### ***1. Ab initio calculations of thermal radiative properties of GaAs in the visible and infrared bands***

It is desirable to control the spectrum and direction of thermal emission in a broad set of thermal management and energy conversion applications, such as in aerospace [1], solar cells [2], thermophotovoltaics [3], optical filters, etc. Selective emission properties can be pursued at multiple scales, expanding from atomic scale to macroscale. Recently, nanostructures have been investigated extensively for their interesting radiative properties, such as antenna effects [4], photonic band gap, and wavelength-selective emission [5]. On the other hand, bulk materials have received much less attention. However, many bulk materials, such as rare-earth oxides [6], also exhibit selective radiative properties due to their special atomic structures. Understanding the relationship between the atomic structure and the macroscopic radiative property can be crucial for designing new bulk materials with desired selective radiative properties, and can offer more design space in addition to making them into various nanostructures.

The fundamental macroscopic material property that determines radiative properties is the dielectric function, which describes the response of a material to a time-dependent external electromagnetic (EM) field. The response to external field (or photons) from far-IR to UV band can be attributed to different mechanisms, including impurity, optical phonon, free carrier, exciton, and interband electronic transition. The relative importance of each mechanism depends on wavelength and material. For example, free electrons dominate the dielectric response in metals almost at all wave length [7]. In contrast, in semiconductors like GaAs studied here, the dominating mechanisms are electronic transitions in the visible band (strictly speaking, from band gap energy to UV band) and optical phonon absorption in the far-IR band. Several dielectric function models have been developed to account for different mechanisms, such as Drude's model for free electrons and Lorentz oscillator model for phonons [7]. However, the parameters in these models are typically obtained from experiments, limiting their applications in predicting radiative properties from atomic structures especially for new materials where experimental data are not available.

With the rapid progress of ab initio methods, the dielectric function models may now be parameterized using ab initio calculations. As such, the relationship between the atomic structure and their radiative properties can be understood using a multiscale simulation approach including ab initio calculations and EM wave theory. Density functional theory (DFT) is a typical ab initio method. Given the initial unit cell structure, it can predict many material properties with a reasonable accuracy, such as equilibrium material structure, electronic band structure, and phonon properties. These results can be used in the dielectric function models to calculate the frequency-dependent dielectric function. EM theory can then be used to calculate radiative properties of bulk materials and nanostructures including photonic crystals, nano-antennas, nanoparticles, etc.

DFT is a quantum mechanical theory to investigate the ground state of many-body systems. In the framework of DFT, many-body systems are treated as systems of interacting electrons in an external potential  $V_{\text{ext}}(\mathbf{r})$ . The ground state energy of the system is completely determined given the ground state electron density  $\rho_0(\mathbf{r})$  only. A functional  $E[\rho]$  for the ground state energy can be defined in terms of  $\rho(\mathbf{r})$ . For a particular  $V_{\text{ext}}(\mathbf{r})$ , the exact ground state energy of the system is the global minimum value of this functional, and the  $\rho(\mathbf{r})$  that minimizes the functional is the exact ground state density  $\rho_0(\mathbf{r})$  [8]. Kohn–Sham (KS) approach further replaces the difficult interacting many-body system with an independent particle system. The single particle KS equations are

$$\left[ -\frac{\hbar^2 \nabla^2}{2m} + V_{\text{KS}}(\mathbf{r}) \right] \varphi_{n\mathbf{k}}(\mathbf{r}) = \varepsilon_{n\mathbf{k}}(\mathbf{r}) \quad (1)$$

with a local effective potential  $V_{\text{KS}}(\mathbf{r})$ , where  $m$  is the mass of the electron,  $\varphi$  is wave function, and  $\varepsilon$  is the eigen-energy. In a periodic solid where the wave vector  $\mathbf{k}$  is a good quantum number, the KS orbitals  $\varphi_{n\mathbf{k}}(\mathbf{r})$  are Bloch states with band index  $n$ , wave vector  $\mathbf{k}$ , and energy  $\varepsilon_{n\mathbf{k}}$ . The ground state density  $\rho(\mathbf{r})$  can be represented by the wave functions using

$$n(\mathbf{r}) = 2 \sum_{v\mathbf{k}} |\varphi_{v\mathbf{k}}(\mathbf{r})|^2 \quad (2)$$

where  $v$  donates the summation of the valence bands.  $V_{\text{KS}}(\mathbf{r})$  is given by

$$V_{\text{KS}}(\mathbf{r}) = V_{\text{ext}}(\mathbf{r}) + V_{\text{H}}(\mathbf{r}) + V_{\text{xc}}(\mathbf{r}) \quad (3)$$

Here  $V_{\text{ext}}$  is the external potential, which is usually the ion–electron interaction potential and can be replaced by a pseudopotential.  $V_{\text{H}}(\mathbf{r})$  is the Hartree potential, which is simply the Coulomb interaction

between electrons and can be determined by electron density  $\rho(\mathbf{r})$ .  $V_{xc}(\mathbf{r})$  is the exchange and correlation potential, which contains many complicated terms, including quantum electron repulsion, electron kinetic energy, electron correlation energy, etc. Many functionals are available to predict the exchange and correlation energy from electron density. Once the KS potential energy is determined, those single particle KS equations can be solved by iterative minimization or other advanced algorithms [8].

Electronic interband transitions dominate the photon absorption at near-IR, visible, and UV bands. The transition probability is determined by the transition matrix element  $p_{ij}^a = \langle \mathbf{kj} | p_a | \mathbf{ki} \rangle$ , where  $p_a$  is in general the operator which couples the initial and final states. In this case,  $p_a$  is the momentum operator. With an integration of transition matrix elements over all the possible vertical transitions across the band gap, the imaginary part of the dielectric function  $\epsilon''(\omega)$  can be determined by the Fermi's golden rule (in atomic units) [9],

$$\epsilon''_{aa}(\omega) = \frac{4\pi^2}{\Omega\omega^2} \sum_{i \in VB, j \in CB} \sum_{\mathbf{k}} w_{\mathbf{k}} |p_{ij}^a|^2 \delta(\epsilon_{\mathbf{kj}} - \epsilon_{\mathbf{ki}} - \omega) \quad (4)$$

where  $\Omega$  is the unit-cell volume and  $\omega$  is photon frequency, VB and CB denote the valence and conduction bands,  $w_{\mathbf{k}}$  is the weight associated with a  $k$ -point, and  $a$  denotes a particular direction. The delta function is used to ensure the energy conservation associated with an electronic transition: only when the photon energy matches the energy difference between a valence and conduction state, the transition can occur. Dirac delta function  $\delta(x)$  can be approximated by a Gaussian function

$$\delta(x) \approx \frac{1}{\sqrt{\pi}\Gamma} \exp\left(-\frac{x^2}{\Gamma^2}\right) \quad (5)$$

The real part of the dielectric function is obtained from  $\epsilon''(\omega)$  by a Kramer–Kronig transformation

$$\epsilon'(\omega) = 1 + \frac{4}{\pi} \mathbf{P} \int_0^\infty d\omega' \frac{\omega' \epsilon''(\omega')}{\omega'^2 - \omega^2} \quad (6)$$

where  $\mathbf{P}$  denotes the principle value of the integral. Once we get the dielectric function  $\epsilon = \epsilon' + i\epsilon''$ , linear optical properties, such as refractive index and absorption spectrum, can be calculated.

The dielectric function in the far-IR band has a different nature, because the dielectric response is determined by the vibrational behavior of ions. Using the response–function formalism within DFT, the second order derivatives of total energy and wave functions of periodic solids with respect to displacement of atoms or homogeneous static electric fields can be calculated [10]. As a result, the parameters such as dynamical matrices, Born effective charges, dielectric permittivity tensors can also be determined. For semiconductors and insulators, the dielectric permittivity tensor is calculated through,

$$D_{mac,a} = \sum_b \epsilon_{\infty,ab} E_{mac,b} \quad (7)$$

where  $D_{mac}$  is the macroscopic displacement field and  $E_{mac}$  is the electric field, and  $a$  and  $b$  denote the directions. Here we use the high frequency dielectric permittivity  $\epsilon_{\infty,ab}$  instead of the static dielectric permittivity  $\epsilon_{0,ab}$  because in DFT calculations the ions are treated as external potential, and only the electronic contribution is included in polarization.

The knowledge of phonon frequencies and eigenmodes is acquired once dynamical matrix is calculated. Since GaAs is isotropic, the dielectric permittivity tensor reduces to a scalar. The frequency-dependent dielectric function  $\epsilon(\omega)$  is calculated by adding the ionic contribution to  $\epsilon_\infty$  (the oscillator model)

$$\frac{\epsilon(\omega)}{\epsilon_\infty} = 1 + \sum_m \frac{\omega_{LO,m}^2 - \omega_{TO,m}^2}{\omega_{TO,m}^2 - \omega^2 - i\gamma\omega} \quad (8)$$

where LO and TO denote the longitudinal and transverse optical phonon modes, and  $m$  goes over all the IR-active modes. Ab initio calculations are not capable of capturing the temperature-dependent damping term  $\gamma$  in the oscillator model, so it is usually neglected or fitted from experiments[11].

First-principle calculations are carried out using the plane-wave pseudopotential method, which is implemented in the ABINIT code[12]. Local density approximation (LDA) is used for exchange and correlation potential with Troullier–Martins pseudopotentials [13]. A primitive cell with one Ga and one As atoms and a large plane wave cutoff of 16 Hartree/Bohr are used. A  $12 \times 12 \times 12$   $k$ -point grid generated in the irreducible Brillouin zone is used for the  $k$ -space integration.

To check the applicability and accuracy of the pseudopotentials, geometry optimization and band structure calculation are first carried out. Since GaAs has a simple zinc-blende structure, the geometry optimization only includes the optimization of lattice constant. The calculated lattice constant and band gap are compared with existing data and listed in Table 1, and the band structure is shown in Fig. 1. The calculated lattice constant is 2% smaller than the experimental value, while the band gap value is similar to experiment. Underestimation of lattice constant is common for GaAs if an LDA based pseudopotential is used without nonlinear-core correction or including d orbitals [14]. Although the lattice constant is underestimated, the standard norm-conserving pseudopotentials give quite decent band structure prediction. Therefore, they are chosen for our calculations.

Table 1. The calculated lattice constant and band gap compared with existing experimental and theoretical data.

Parameters	Lattice constant (Å)	Band gap (eV)	Refer ence
This work	5.45	1.54	
Previous prediction	5.654	1.04	[15]
Experimental data	5.65	1.52	[16]

To obtain the dielectric function within near-IR to UV region, the band structure is analyzed using the ABINIT component optic program, based on Eq. (4). The spectral dielectric function from 0 to 8 eV is shown in Fig. 2. The imaginary part of the dielectric function is zero below 1.54 eV because no absorption occurs below the gap energy. There are three peaks around 3, 5, and 6 eV, which can be attributed to the optical transition near the L and X point in the Brillouin zone [17]. Our prediction matches the second and the third peaks pretty well, while the location and height of the first peak is not well-predicted. The failure to accurately predict the first peak height is also seen in other calculations [18] and is due to the neglecting of excitons.

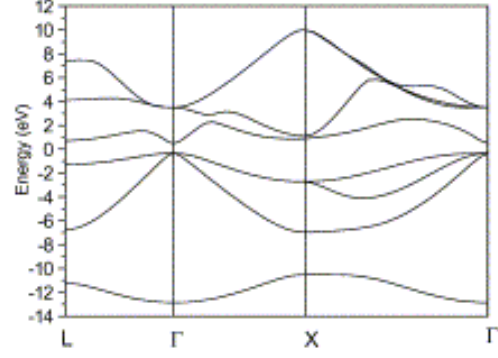


Fig. 1. The calculated electronic band structure of GaAs.

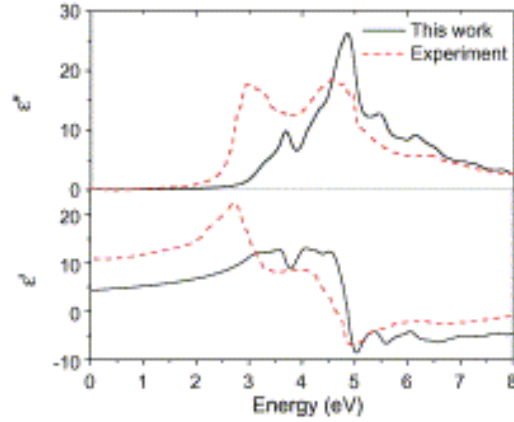


Fig. 2. Our calculated imaginary and real parts of the dielectric function for GaAs from near-IR to UV bands, as compared to experimental data from Ref. [19].

The calculation of IR permittivity tensor using response-function formalism is also implemented in ABINIT. This approach includes a self-consistent calculation to obtain the charge density, a non-self-consistent calculation to obtain the wave function, and a calculation to generate derivatives of the 1st, 2nd, or 3rd orders with respect to the electric field and the atomic displacement. The static dielectric tensor and dynamical matrices are then obtained. The phonon frequencies and vibrational mode are calculated by diagonalizing the dynamical matrix. The calculated static and high frequency dielectric permittivity and optical phonon frequencies are shown in Table 2. The calculated dielectric permittivity for zero and infinite frequencies are slightly overestimated compared with experimental results, presumably due to the underestimation of the lattice constant. GaAs has a zinc-blende structure, which has only two atoms in a primitive cell and only three optical phonon branches. The calculated zone-center optical phonons frequencies match the experimental value well. Normal mode analysis [20] of zone-center optical phonon indicates that this phonon mode has an  $F_2$  symmetry, which is both Raman and IR active. The photons have much smaller momentum than phonons, so only the interaction with zone-center photon needs to be considered. The spectral dielectric function from 0 to  $800\text{ cm}^{-1}$  is then calculated using the oscillator model and shown in Fig. 3. Damping is neglected here, so the dielectric function is real. Only one peak is observed because there is only one IR-active phonon mode in GaAs.

Table 2. The calculated static and high frequency dielectric permittivity and phonon frequencies (with  $F_2$  symmetry) compared with experimental data.

Parameters	$\epsilon_0, \epsilon_\infty$	$F_2(\text{TO,LO})$ ( $\text{cm}^{-1}$ )	Reference
Our prediction	15.77, 12.85	257.7, 267.5	
Experimental data	13.63, 10.88	271.1, 285.2	[21]

The calculated reflectance is compared with experimental data [22], as shown in Fig. 4. We choose the low-temperature experimental data because our calculation is performed at 0 K. Overall our data agree well with the experiment. In the IR region, one reflection peak appears which can be attributed to the strong optical phonon oscillation. Compared with the experiment, the calculated reflection peak is higher and reaches one due to the neglect of damping. The reflectance at the plateau between phonon absorption and electron absorption is also similar to experimental results indicating an accurate prediction of high frequency dielectric constant ( $\epsilon_\infty$ ). From near-IR to UV range, the reflectance peaks correspond to large interband absorption.

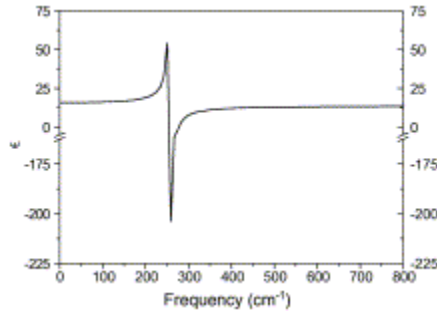


Fig. 3. The calculated IR dielectric function for GaAs.

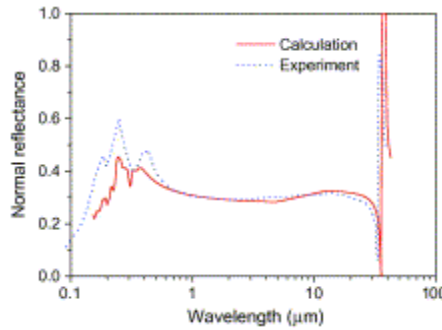


Fig. 4. The calculated reflectance over the entire spectrum compared with experimental data.

To summarize, the theoretical framework of calculating radiative properties from ab initio methods is presented, using GaAs as an example. Fermi's golden rule is applied to analyze the band structure and determine the spectral dielectric function for near-IR to UV band. Far-IR reflectance is calculated by analyzing the derivatives of energy and wave function with respect to external electric field and atom displacement. This approach can be used to obtain the reflectance using the atomic structure as the only

input. Similar calculations can be performed to predict the optical properties of other bulk materials, and some nanostructures such as small nanoparticles.

## 2. *Ab initio* calculations of the dielectric function of SWCNT

The individual dielectric tensors of a set of SWCNTs with varying chirality are first calculated from first-principles. The dielectric tensors of the CNTs are then assigned to spatial domains within electrodynamics simulations of the macroscopic array. In this way, the effective optical properties of the macroscopic array can be calculated for a defined array geometry.

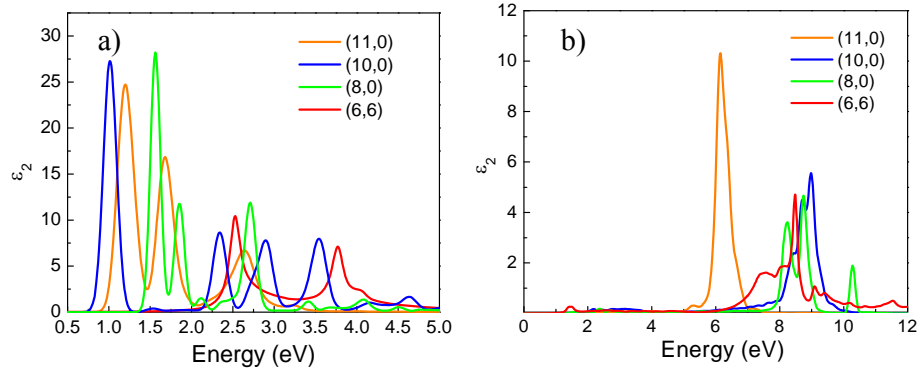


**Fig. 5** GW-BSE absorption spectra of SWCNTs for a) s-polarization and b) p-polarization with a broadening of 0.80 eV

The first-principles approach initially involves the calculation of the ground-state wavefunctions and eigenvalues of the Kohn-Sham equations within the local density approximation (LDA). We use a planewave basis with a cutoff of 100 Ry and Troullier-Martins norm-conserving pseudopotentials [23], with a convergence threshold of  $1 \times 10^{-6}$  Ry for self-consistency. An increased planewave energy cutoff is necessary for convergence of iterative block-diagonalization methods such as the Davidson method [24], so that the number of states to be calculated is much smaller than the dimension of the basis set. At least 10 Å vacuum space is included in the radial directions to minimize interactions with periodic images. 32 k-points are used for the DFT and GW calculations and 400 k-points are used in the BSE calculations. The long-range coulomb interaction arising from the 1-D structure of CNTs is truncated based on a cylindrical geometry that has been documented previously [25]. This is done to ensure that intertube interactions do not influence the calculated dielectric function because the intertube separation in experiments is much larger than the characteristic CNT diameter. Precise control of chirality in macroscopic SWCNT arrays is still elusive in experiments. As a result, the inhomogeneity inherent in macroscopic arrays must be accounted for in order to understand and optimize the optical properties of the array. We calculate the dielectric function of a normal distribution of SWCNTs with mean diameter 0.72 nm and standard deviation 0.6 nm. The chiralities are chosen in consideration of computational cost to be either armchair or zigzag due to their decreased unit cell size. The dielectric tensors are calculated for each chirality within the GW-BSE method and the resulting imaginary part for light polarized parallel (s-polarization) and perpendicular (p-polarization) to the CNT axis are shown in Figure 1. Comparison of the first and second absorption peaks from GW-BSE with experiments shows excellent agreement, validating the use of this first-principles method [26]. The results for the (6,6) metallic CNT are in agreement with GW-BSE calculations of other small-diameter, metallic SWCNTs [27]. Figure 5 also reveals strong absorption peaks in the near IR and visible spectra for s-polarization. Further, the absorption peaks for the (6,6) metallic CNT are higher in energy than those of the semiconducting CNTs. Previous tight binding calculations have predicted that the first absorption peaks of metallic CNTs are higher in energy than those of semiconducting CNTs of similar diameter [28]. For p-polarization, the



optical transitions at lower energies are forbidden, resulting in absorption peaks in the UV spectrum. The anisotropic nature of the optical absorption spectra in SWCNTs has been studied extensively [29].

**Table 3.** Energetic positions of first and second absorption peaks for s-polarization

	GW/BSE ( $E_{11}$ , $E_{22}$ ) (eV)	Exp. ( $E_{11}$ , $E_{22}$ ) (eV) [27]
(11,0)	1.18, 2.67	1.21, 2.69
(10,0)	1.01, 2.34	1.11, 2.36
(8,0)	1.56, 1.85	1.62, 1.88
(6,6) – metallic	2.53, 3.77	--

### 3. *Electrodynamics simulations of radiative properties of SWCNT arrays*

The solution of Maxwell's equations subject to boundary conditions forms the basis of electrodynamics simulations. Here, we use the finite element method to solve these equations in the differential form for a time-varying electric field in 3-dimensional space.

$$\nabla \times H = J + \frac{\partial D}{\partial t} \quad (9)$$

$$\nabla \times E = -\frac{\partial B}{\partial t} \quad (10)$$

$$\nabla \cdot D = \rho \quad (11)$$

$$\nabla \cdot B = 0 \quad (12)$$

The coupling between the electronic structure calculations and electrodynamics simulations can be defined explicitly by relating the electric displacement to the electric field intensity:

$$D = \epsilon_0 \epsilon_r E \quad (13)$$

where  $\epsilon_r$  is the relative permittivity.

The imaginary part of the relative permittivity, the dielectric tensor for anisotropic materials, is calculated within the GW-BSE method as:

$$\epsilon_2(\omega) = \frac{16\pi e^2}{\omega^2} \sum_s \left| \vec{\lambda} \cdot \langle 0 | \vec{v} | S \rangle \right|^2 \delta(\omega - \Omega_s) \quad (14)$$

where  $\lambda$  is the polarization vector,  $v$  is the single-particle velocity operator and  $\Omega_s$  is the excitation energy. The real part of the relative permittivity is then calculated using the well-known Kramers-Kronig relations. Depolarization effects cause the CNT optical response to be significantly suppressed for light polarized perpendicular to the CNT axis [30, 31]. This necessitates the calculation of the diagonal frequency dependent elements of the dielectric tensor from first-principles.

Electrodynamics simulations are performed with light incident on an array, with the length of the material in the surface normal direction corresponding to the array thickness. The incidence angle as well as simulation domain are illustrated in Fig. 6. The array is treated as a homogeneous, effective material, with the dielectric tensor defined within effective medium theory. The effective dielectric function for the macroscopic array is calculated using Maxwell-Garnett (MG) effective medium theory [32]. The MG expression for the effective relative permittivity is:

$$\epsilon_{eff,k} = \epsilon_0 + \frac{\sum_i \frac{f_i(\epsilon_i - \epsilon_0)}{\epsilon_0 + N_{i,k}(\epsilon_i - \epsilon_0)}}{1 - \sum_i N_{i,k} \frac{f_i(\epsilon_i - \epsilon_0)}{\epsilon_0 + N_{i,k}(\epsilon_i - \epsilon_0)}}, \quad (15)$$

where the background permittivity,  $\epsilon_0$ , is taken to be that of air. The summation is over all CNTs included in the effective material, with  $f$  being the volume fraction of each and index  $k$  corresponding to the light polarization vector.  $N$  is the depolarization factor, which depends on the polarization of light and geometry of the dielectric inclusion. Here, it is taken to be  $\frac{1}{2}$  for s-polarization and 0 for p-polarization, as defined for a thin rod geometry [33]. The use of MG theory was validated by comparing the calculated absorption spectra of the effective material with that of an inhomogeneous array with the geometry of individual CNTs defined using a Monte-Carlo method of spatial distribution. Both treatments of the macroscopic array account for inhomogeneity in the spatial CNT distribution and assume well-ordered arrays with the CNT axes perfectly aligned. Due to the absence of classical resonance effects, it was found that the calculated absorption spectra were identical. The effective medium approach was used in all subsequent results, as it is significantly less computationally expensive than the Monte-Carlo approach. The inhomogeneity in the CNT distribution is defined in MG theory simply through the volume fraction corresponding to each CNT in the array. General CNT growth processes produce arrays with approximately 33% metallic CNTs [34]. The volume fractions of the four semiconducting CNTs were set equal to each other such that the total volume fraction of CNTs defined the desired array density. This quantity was set to 3% to simulate relevant experimental conditions for SWCNT arrays [35]. The density of metallic CNTs relative to the total number of CNTs was fixed at 33% for all subsequent calculations.

The optical properties of the macroscopic array have been calculated for an arbitrary incidence angle of 45 deg and array thickness 1  $\mu\text{m}$ . The calculated quantities absorptance, reflectance and transmittance are shown in Fig. 7. Absorption and transmission clearly dominate the response of the material, with reflectance remaining below 0.05 over the entire spectral range. The peaks and shoulders in the absorptance relate directly to peaks in the calculated  $\epsilon_2$  for both polarizations resulting from components of the electric field both parallel and perpendicular to the CNT axis. Absorption at energies below 5 eV corresponds to peaks in  $\epsilon_2$  for s-polarization, whereas the peak at 7 eV is attributed to the peak in  $\epsilon_2$  for p-polarization. The extremely low reflectance and relatively high absorption are indicative of the blackbody behavior of the material.

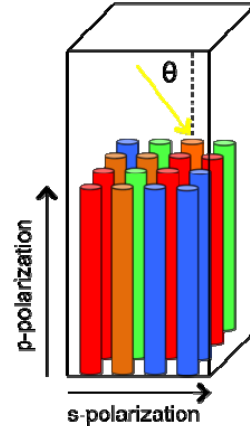


**Fig. 6.** Electrodynamics simulation domain and incidence angle.

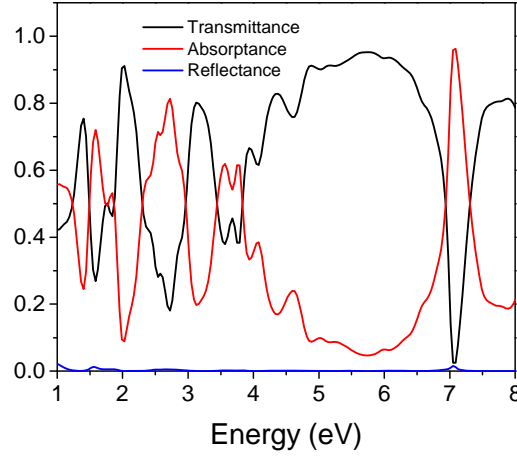


**Fig. 7.** Calculated optical properties of macroscopic array with thickness of 1  $\mu\text{m}$

Although it is clear that the array achieves minimal reflectance in the near IR and visible spectra, the anisotropy in the optical properties of individual CNTs has the potential to adversely affect these results. However, the vertical alignment of the CNTs ensures that the reflection of p-polarized light accounts for the total measured reflection, whereas reflection of s-polarized light is confined inside the material as it is gradually absorbed. The reflectance of p-polarized light can be described by calculating the effective index of refraction from the real and imaginary parts of the effective dielectric function for light polarized perpendicular to the CNT axis. The results corroborate the suggestion that the total reflectance is dependent on the effective dielectric function for p-polarized light. The low absorption of p-polarized light and effective index of refraction close to that of air at lower energies indicates that the material is significantly more transparent to this polarization than s-polarization. Therefore, light is able to propagate through the material as the components with s-polarization are absorbed. Figure 8 shows the effective index of refraction and absorption spectra for three densities, with the 3% volume fraction corresponding to an intertube separation of 15 nm, and the higher density corresponding to an intertube separation of 4 nm. The extremely low index of refraction is unusual for bulk materials and results from the array's sparsely aligned nanostructures. It is apparent that as the density is increased, the index of refraction for p-polarized light increases, leading to an overall increase in the reflectance in the surface normal direction. Furthermore, the absorption spectra for s-polarization shows increased intensity of absorption peaks corresponding to stronger volumetric absorption within the composite material. However, the blackbody behavior of the material is not retained at higher densities and the increased absorption is accompanied by increased reflection for both polarizations.

In summary, we have developed a generalized computational method of predicting the optical properties of inhomogeneous, nanostructured materials. This method, applied to the properties of macroscopic SWCNT arrays, has resulted in a fundamental understanding of the mechanisms leading to the unique blackbody behavior of the material. The computed properties of the array are in agreement with previous experiments and the simulations have been used to extend experimental findings to modify the optical properties based on geometric parameters of the array. These results suggest that the blackbody behavior of these materials is a direct result of both the atomic and microscopic structure of the CNTs and array, respectively. As discussed previously, the effective material is virtually transparent to p-polarized light, but strongly absorbs s-polarized light. Because of the low CNT density, the index of refraction for p-polarized light is significantly lower than other low-index of refraction materials. This property decreases reflection of light in the surface normal direction and allows the light to propagate through the material and gradually become absorbed.

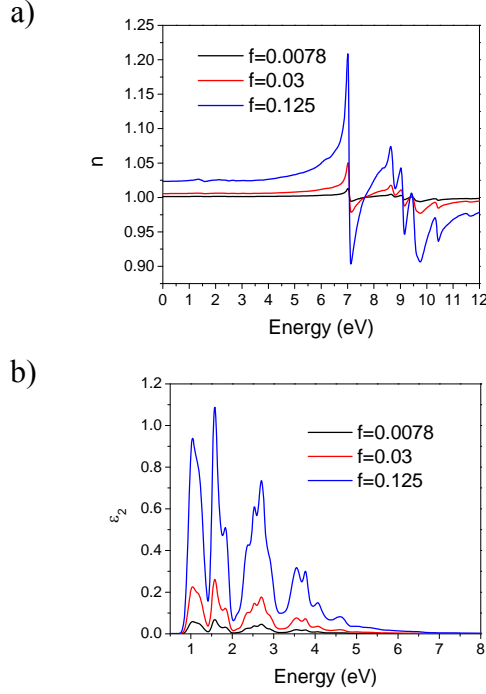


**Fig 8.** MG theory calculations of a) index of refraction for p-polarized light and b) imaginary part of the dielectric function for s-polarized light.

#### 4. Finite difference time domain (FDTD) simulations of radiative properties of MWCNT arrays

The ordered vertical array of MWCNTs considered in this work is shown in Fig. 9. The CNTs are aligned along the  $z$  direction and the array forms a 2D square lattice in the  $xy$  plane. The surrounding media is simply the air. Normal or oblique incidence illuminates the array from the top. In our calculations, a CNT is treated as a roll of graphite and the local dielectric tensor is given by [36]

$$\epsilon(\hat{r}, \hat{\phi}, \hat{z}) = \epsilon_e \hat{r}\hat{r} + \epsilon_o(\hat{z}\hat{z} + \hat{\phi}\hat{\phi}), \quad (16)$$

Clearly, this dielectric tensor has nondiagonal components in the Cartesian coordinate, which makes it difficult to be applied in FDTD calculations. It is thus further simplified to a diagonalized form within the effective medium approximation. The components of the dielectric tensor are then given by

$$\begin{aligned} \epsilon_{\parallel} &= \epsilon_o \\ \epsilon_{\perp} &= \sqrt{\epsilon_e \epsilon_o}. \end{aligned} \quad (17)$$

where  $\epsilon_{\parallel}$  and  $\epsilon_{\perp}$  are the components of the dielectric tensor parallel and perpendicular to the CNT axis, respectively. We adopted the graphite properties from Ref. [37] and calculated the dielectric tensor of an individual CNT using Eq. (17). Once the dielectric tensor of an individual CNT is obtained, the FDTD method, implemented in the Meep package [38], can be carried out to obtain reflectance, transmittance, and absorbance of CNT arrays. The spatial resolution  $x$  is chosen to be 5 nm after the convergence test,

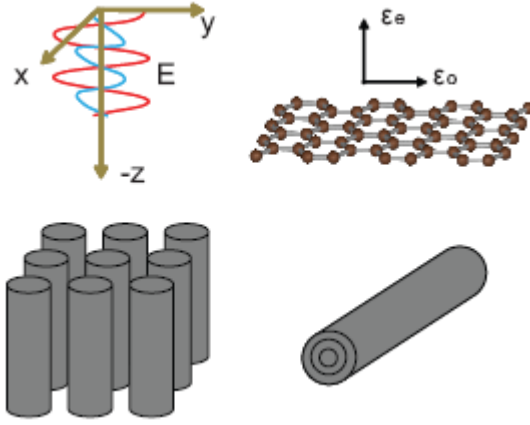


Fig. 9 Left: A sketch of a CNT array subject to normal incidence. Upper right: single layer graphite and the anisotropic dielectric tensor. Lower right: MWCNT as a roll of multilayer graphite.

and the time step is given by  $t = 0.5x/c$ , where  $c$  is the speed of light. Periodic boundary conditions are applied in both  $x$  and  $y$  directions of the simulation domain, so that a cell with only one CNT within is needed to model an infinitely large CNT array. Narrow-band Gaussian pulses centered at different frequencies are generated at the incidence plane and Fourier transforms are applied to calculate the energy flux at each central frequency. Here since nonlinear effects are not included in numerical calculations, components at other frequencies in the Gaussian pulse do not affect the energy flux at the central wavelength. The incident frequencies are corresponding to wavelength from 400 to 850 nm. As mentioned earlier, MGT as a simpler approach was used to predict the optical properties of CNT arrays in most existing studies. In this work we also use MGT approach to obtain radiative properties, and then compare the results to those of FDTD simulations. Different from our cylinder array model, MGT treats the CNT array entirely as an effective homogeneous medium. Because the CNTs are anisotropic and aligned along a particular direction, the effective medium is optically anisotropic. The components of the effective dielectric tensor of such a medium with CNT volume fraction  $f$  are given by

$$\begin{aligned}\epsilon_{eff\parallel} &= 1 + f(\epsilon_{\parallel} - 1) \\ \epsilon_{eff\perp} &= 1 + \frac{f(\epsilon_{\perp} - 1)}{1 + \frac{1}{2}(\epsilon_{\perp} - 1)(1 - f)}\end{aligned}\quad (18)$$

where  $\epsilon_{eff\parallel}$  and  $\epsilon_{eff\perp}$  are the components along the CNT direction and perpendicular to the CNT direction, respectively. These equations are equivalent to Eqs. (7) and (8) in Ref [39]. Thermal radiative properties of these homogeneous mediums can be calculated by analytical methods, which involve calculating the multiple reflection between the upper and lower surfaces. Here for convenience we simply perform FDTD calculations to these mediums and obtain the reflectance, transmittance, and absorbance. The results obtained in this way are denoted by "MGT" in the following sections.

The structure of a nanotube array is characterized by many parameters, which narrow down to tube diameter, intertube distance, and tube length for two-dimensional square lattice. Intertube distance and tube diameter are sometimes combined to define the volume fraction. In our calculations, the typical diameters of MWCNTs are from 40 to 240 nm, the intertube distances vary from 200 to 600 nm, and the tube lengths are from 1  $\mu$ m to 3  $\mu$ m. Very long CNTs are approximated by truncating the CNTs using a perfect match layer (PML). In addition, different incident angles are considered. In the subsections, we will discuss how these parameters affect the optical properties of the CNT arrays. The effects of each parameter are investigated while others are fixed. Four parameters are discussed in sequence: volume

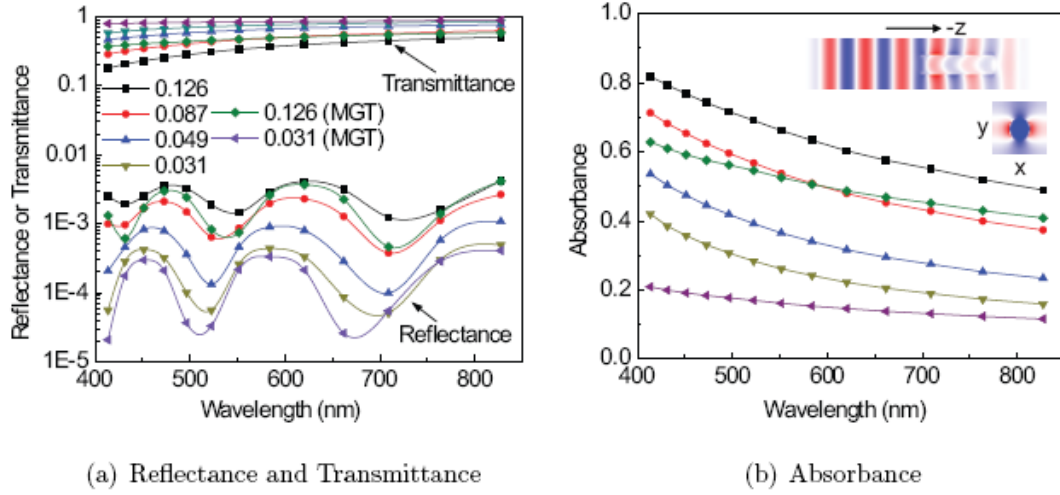


Fig. 10 (a) Reflectance and transmittance and (b) absorbance of the CNT array from FDTD calculation and MGT with different volume fractions. The reflectance and transmittance are shown in a log scale plot. Insert: an instant electric field distribution of the cross sections of the simulation domain with 500 nm incident wave length and 0.126 volume fraction. The upper figure is scaled in the vertical direction for clarity.

fraction, tube length, tube diameter, and incident angle.

The calculated reflectance, transmittance and absorptance for different volume fractions are calculated and shown in Fig. 10. For comparison, the optical properties for  $f = 0.126$  and  $0.031$  calculated from MGT are also shown. Compared to the results of FDTD, both reflectance and absorbance evaluated using MGT are smaller for same volume fraction. For example, when the volume fraction is  $0.031$ , MGT underestimates the absorbance by up to 50% at 413 nm incidence. This indicates that the nano-scale inhomogeneity of the cylinder array structure is very important to its optical properties. As shown in the inserted figure in Fig. 10, the field distribution is not uniform in the cross section perpendicular to the propagation direction. Possible multiple scattering of light within the cylinder array structure is captured in our calculation but not in the homogeneous medium treatment. The scattering could elongate the optical path of photons and result in field enhancement, which greatly enhances absorption[40]. Also, for normal incidence the  $\epsilon_{\parallel}$  component does not contribute to absorption in the MGT treatment, since the electric field is always perpendicular to the tube axis in this homogeneous medium approximation (see Eq. 3.10). In FDTD, however, because the CNT array is not entirely homogeneous, the wavefront is no longer a simple plane, as shown in the inserted figure in Fig. 10. Diffraction can induce electric field with component parallel to the tube axis, so the large  $\epsilon_{\parallel}$  component can also contribute to the absorption. Besides absorption, larger reflectance than MGT is also seen in our results. It can also be attributed to the multiple scattering within the CNT array and electric field component that is parallel to the tube axis. The multiple scattering increases the chance of back scattering and thus the total reflectance. The electric field component parallel to the tube axis can have larger reflectance because of the larger real and imaginary part of  $\epsilon_{\parallel}$ .

It is also necessary to study the angular dependence for two reasons. First, for practical applications, oblique incidence is usually inevitable. Second, in the real CNT arrays, the CNTs are not perfectly vertically aligned and misalignment always exists. Although our calculations predicted CNT arrays to have low reflectance at normal incidence, it is necessary to check how much it changes due to variation of incidence angle or tube misalignment. Unlike the normal incidence case, the transverse electric (TE) and transverse magnetic (TM) waves should be considered separately. The incident angles from  $0^\circ$  to  $70^\circ$  are

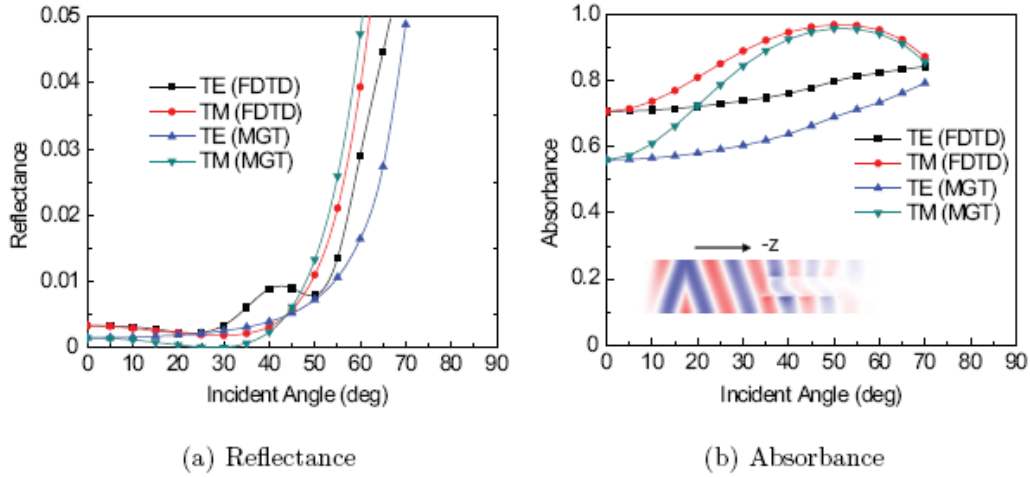


Fig. 11: (a) Reflectance and (b) absorbance of CNTs at different incident angle. Insert: an instant field distribution for TE wave under 20° oblique incidence. The figure is scaled in the vertical direction for clarity.

considered. Even larger angles are not considered due to the numerical difficulty. The polar angle is simply fix at  $0^\circ$ , because previous calculations of silicon nanowire array show that the polar angle will not affect the results much[41]. This means that the projection of the incident ray on the xy-plane is always along the x direction. The tube diameter is 80 nm, the intertube distance is 200 nm, the tube length is 1  $\mu\text{m}$ , and the incident wavelength is 500 nm. The calculated angular dependent reflectance and absorbance are compared with the MGT and shown in Fig. 11.

For a general homogeneous medium, the reflectance of the TE wave increases with angle monotonically to 100%. On the other hand, the reflectance of TM wave will drop to 0 at Brewster angle and then increases to 100% at  $90^\circ$ . The predicted reflectance by MGT follows to this trend. In contrast, the FDTD results of CNT array show that the reflectance of both TE and TM waves first slightly decreases at small angle and finally become very large. This indicates that compared to normal incidence, a small incident angle or small misalignment of the CNTs can further reduce the reflectance. Also, the reflectance of TE waves oscillates and drops to a local minimum at around  $50^\circ$ , which is probably due to the antenna effect of the relatively short CNTs. One effect can be resolved by both FDTD and MGT is that the TM wave shows larger reflectance than TE wave at large angle. This is because TM wave has an electric field component along the tube axis direction and thus is easier to get reflected. The angular-dependent absorbance of TE wave increases with incident angle in the range we considered. For TM wave, the absorbance reaches a maximum at around  $50^\circ$  and then decreases. The MGT predicts similar trends but smaller values. The underestimation of MGT is still due to the neglecting of scattering in the homogeneous medium assumption. To understand the angular-dependent absorption, two angular regions should be considered separately. When the incident angle is small, the reflectance is negligible and almost all incident light can enter the medium. The absorption increases with incident angle due to the longer path the wave travels before it gets transmitted. When the angle is large, the reflectance starts to increase dramatically. Although the optical path becomes longer, less light can enter the medium because of the large reflectance. The competition of increasing reflection and increasing optical path gives the maximum in the absorbance curve for TM wave around  $50^\circ$ . The absorbance of TE wave does not show a maximum only because it is difficult to perform similar calculations at very large incident angles. In fact, a maximum absorption angle is still expected because the reflectance will eventually become 100% for  $90^\circ$  incidence and the absorbance will drop to zero. Also, TM wave shows a larger absorption than TE wave since it has an electric field component parallel to the tube axis along which the imaginary part of the dielectric function is larger.



## **5. Effects of structural randomness on the radiative properties of MWCNT arrays**

Most studies of optical properties of carbon nanotubes are done on ordered array of MWCNT [35, 42] which is always only an ideal situation. Randomness is inherent to any fabrication process so it becomes very essential to gauge the effects of different structural randomness on the radiative properties of MWCNT as a lot of effort goes into making the array more ordered[43, 44] which might not be very necessary to enhance their optical properties[45, 46]. Structural randomness can essentially be classified using parameters such as CNT diameter, length, position and orientation[47]. In this part each of the structural randomness is dealt with separately to find out which randomness has a predominant effect on the absorptive and reflective properties of the array. In each of the cases randomness is introduced in only one of the parameters while the other parameters are kept constant and simulation is carried out and the results are then compared to an ordered array of MWCNT. This helps in analyzing what difference that particular parameter is bringing about in the optical properties. The study of structural randomness is very important not only because this is much closer to real life scenario but also because it changes the whole dynamics of the problem as the properties such as the dielectric constant vary with position in the array thus introducing localization effects. Similar studies were carried out for arrays of silicon nano wire arrays[45, 48] which showed that randomness indeed has an effect and in this case an enhancing effect on the absorptive properties of the array. The randomness in MWCNT arrays has a very different effect on the absorptive properties as the dielectric constant of MWCNT [48, 49] is different from that of silicon nanowires as it is much more absorptive in nature. A brief description of the simulation model is given and the results obtained from simulation on different types of structural randomness in arrays of MWCNT are analyzed in the sections below.

The simulation domain is square of 400 times 400 nm in the XY plane (periodic both in the X and Y direction) and 3100 nm in the Z direction (truncated by PML at the top and bottom). The simulation domain contains 16 CNTs this gives us a surface filling fraction of 12.5 percent in all the cases. No substrate is placed below the array. A Gaussian source is placed at around 1500 nm above CNTs upper surface. Two power monitors placed above and below the array are used to measure the transmitted and reflected flux the values which are then normalized by the source power. For all the cases the reflectivity and transmissivity are calculated between wavelengths of 400-800 nm with an 8 nm resolution which covers the entire visible spectrum. The simulations are run for a 1000 fs time duration and a spatial resolution  $\Delta x=5$  nm is chosen for the simulation mesh. For all the cases five different configurations are sampled and transmissivity and reflectivity values are averaged and the results are compared to the ordered array case. The absorptivity is thus calculated using  $A=1-T-R$  where T and R are the transmission and reflection calculated from the simulation. The above simulations are carried out using commercial software called Lumerical [50].

Randomness in the diameter of the order of 20 nm is introduced such that the maximum and the minimum diameter in the array vary between 30-50 nm. The surface filling fraction of this array is matched to that of an ordered array in which the CNT diameter is fixed at 40 nm. Random diameter arrays show a slight improvement of nearly 5-8 percent in the absorptivity but there is no change in the reflectivity of the array. The increase in absorptivity could be because of higher diffraction of light at the upper surface of the array as compared to an ordered array which is indicated by Fourier transform of electric field just below the surface of the array showing enhanced electric fields around the MWCNT. This is different from what we see in a silicon wire where the enhancement in absorption in the random diameter array is dominated by internal resonance in the nanowire which is very diameter sensitive. We do not see this happen in MWCNT because they are very absorptive in nature and the light rays are usually absorbed in a single pass through the array. Reflectivity in the array is primarily only due to reflection at the topmost surface as the reflection from the bottom surface is completely absorbed so it is only a function of the surface area which interacts with the incident light. As the surface filling fraction is same for both the random and ordered array we do not see any change in the reflectivity pattern.



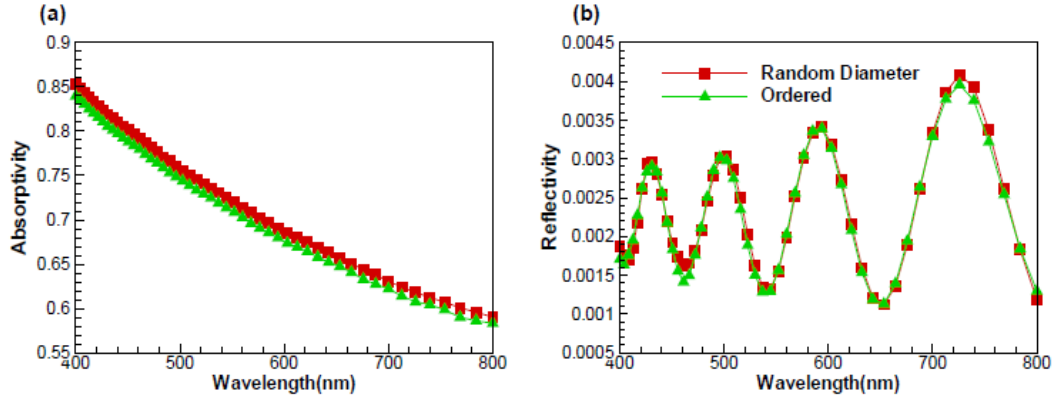


Fig. 12: (a) shows the absorptivity of random diameter array in comparison to the ordered array and we can clearly see an increase in absorption Figure(b) shows the reflectivity of Random Diameter array case and we can see that the reflectivity as compared.

Ordered arrays have very low reflectivity when due to the very low surface filling fraction but to further suppress the reflectivity without affecting the absorptivity it is needed that the surface filling fraction at the topmost layer be lesser but the total volume fraction not decrease[51, 52]. This can be achieved by having an array of MWCNT with variable length. In this simulation the length of each of the MWCNTs is varied between 1000-2000 nm such that the average length of the overall array is till around 1500 nm so the total volume fraction is same as that of an ordered array with all the MWCNTs at 1500 nm length. Since the total absorptivity is dependent on the volume fraction we do not see a signification change from that of an ordered array. But since the surface filling fraction changes along the length of the array with the lowest being at the top most point we see that reflectivity is suppressed substantially as shown in the figure below. The reflectivity pattern is also not sinusoidal and is almost wavelength independent since light is reflected from different lengths of CNT. Even though we see enhanced diffraction in this case too we do not see any enhanced absorptivity because absorption is mainly because of multiple interaction and trapping of the diffracted light rays between the MWCNT. But in random length arrays diffracted light from the top surface might have to travel long distance before interacting with another CNT.

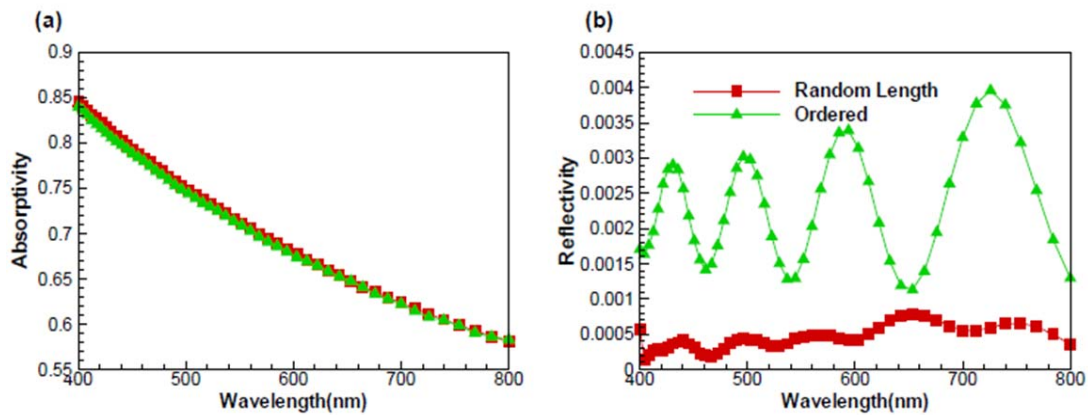


Fig. 13: (a) The absorptivity for the random length case does not differ from the ordered array case; (b) Reflectivity of the random length array is an order of magnitude less compared to that of an ordered array.

Random positioning of MWCNT in the array is the probably the most commonly found defect in fabrication. To replicate this in design the simulation domain is made into smaller cells of 100X100

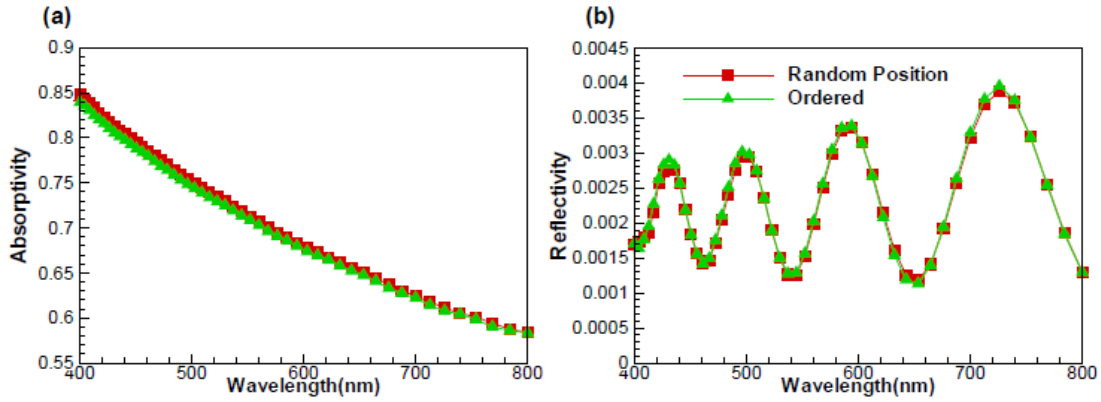


Fig. 14: (a) shows the absorptivity of random position arrays we can see a slight increase in absorption at lower wavelengths. Figure (b) shows the reflectivity which is very similar to the ordered array.

dimension and each one of the MWCNTs are positioned randomly inside these smaller cells. In this design some MWCNT are closer and some are placed much farther thus the effects of multiple scattering and trapping of light get enhanced at some places more than others. Also the dielectric function changes locally along the XY plane of the array. In such arrays high localization of electric fields is observed at some points in the array but this is evened out because of lower electric fields at other places in the array. Thus the absorptivity of such arrays is very similar to that of ordered arrays. Since there is no change in the surface filling fraction the reflectivity of the random position arrays is similar to that of an ordered array. Similar trends were observed for silicon wire arrays too with only very slight enhancement in absorptivity. So investing time in trying to make the array more ordered does not really help in changing either absorptivity or reflectivity of the array.

Since the MWCNT are very long as compared to their diameter there could be a leaning of the ends MWCNT which is simulated by giving an angle of orientation to the MWCNT. In this simulation the CNT are randomly oriented only at very small angles of inclination of nearly 5-10 degrees from the vertical. At such low angles of inclination an increase in absorptivity is observed since most of the light incident on the array is redirected into the array after being reflected from the inclined CNTs which also causes enhanced multiple scattering of light. Slightly lower reflectivity is observed because of the same above reason and a very rough top surface.

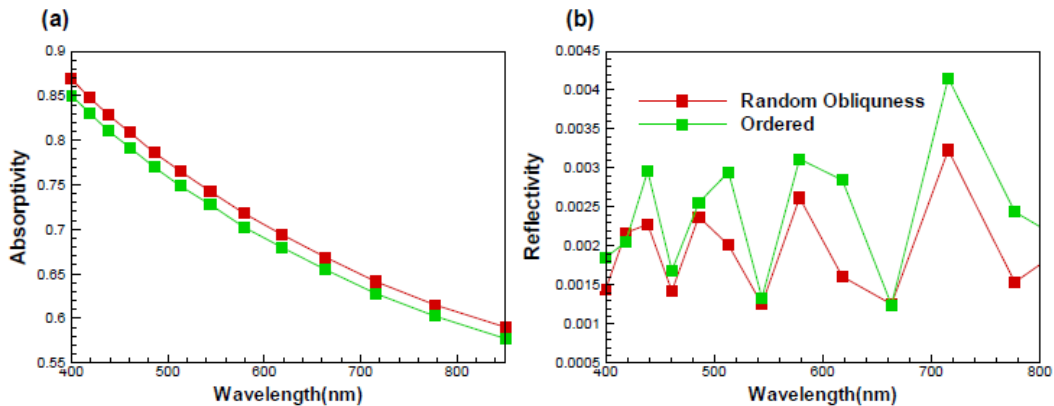


Fig. 15: (a) shows absorptivity in the randomly oriented array higher as compared to the ordered array. Figure (b) shows the reflectivity of the random array is lower as compared to ordered arrays.

In summary, from the simulations carried out on each of the different structural randomness we can conclude that in arrays of MWCNT randomness in diameter and orientation causes enhancement in absorption as compared to ordered arrays. Random length arrays show significantly reduced reflectivity and random oriented array show slightly reduced reflectivity as compared to ordered arrays. Random position arrays show very similar trends to that of an ordered array. From this work it is clear that putting extra effort to eliminate these above stated randomness is unnecessary and in most cases randomness is beneficial in enhancing the optical properties of MWCNT .

## 6. Enhanced absorption in random vertical silicon nanowire arrays

Silicon nanowire (NW) arrays have received considerable attention recently for solar cell applications [53]. The radial p–n junction can enable efficient carrier collection [54], and the open array structure can significantly enhance optical absorption [41]. Absorption enhancement can be attributed to three major mechanisms. First, the NW array structure has remarkably small reflectivity owing to the large open area on the frontal surface. Second, each individual NW is a nanoscale cylindrical resonator, which can trap light by multiple total internal reflections [55]. Third, strong interwire light scattering occurs to cause further light trapping, because the NW diameter and period are normally of the same order as the optical wavelength. These mechanisms are quite sensitive to structural parameters of the NW array. So far, most experimental and all theoretical works have concerned ordered arrays with uniform NW diameter and length [56]. However, various types of structural randomness, such as random NW position, diameter, length, and orientation, are inevitable in experimentally synthesized devices. In fact, a few experiments have been performed on NW arrays with random orientation (and probably random length, diameter, and position as well) [57, 58], and increased reflection or backscattering is generally observed but the effects on absorption are not clear. On the other hand, our previous studies on a random one-dimensional multilayer and two-dimensional cylinders have indicated significant absorption enhancement due to photon localization in random media [40]. Therefore, it is necessary to evaluate whether each type of structural randomness will deteriorate the excellent absorption of NW arrays or, on the other hand, has the potential to further enhance absorption. Here, we numerically investigate the impacts of three types of structural randomness on light absorption, including random position, diameter, and length. The reflection, transmission, and absorption of these NW arrays are predicted and compared with those of ordered arrays.

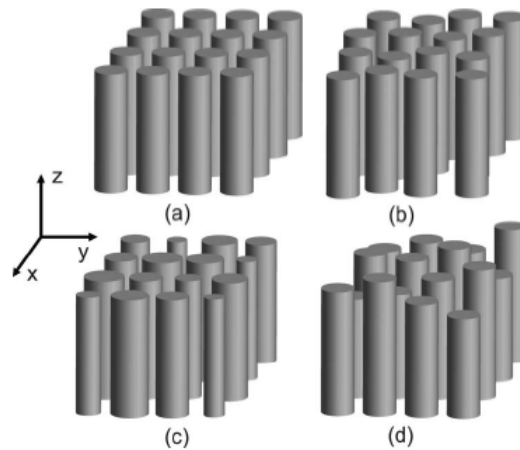


Fig. 16: Sketches of ordered and random arrays: (a) ordered, (b) random-position, (c) random-diameter, and (d) random length.

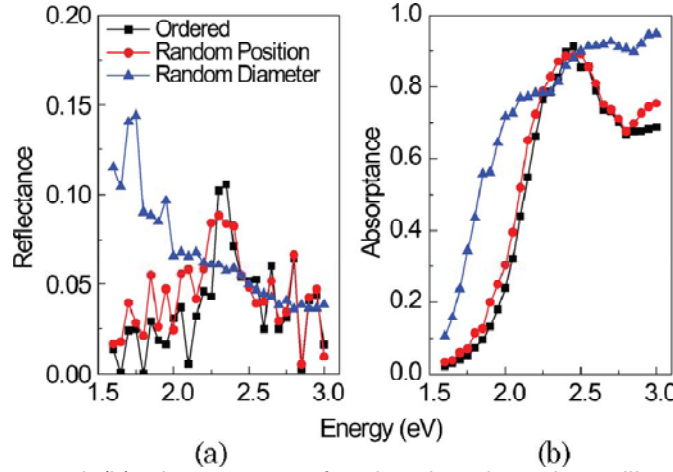


Fig. 17: (a) Reflectance and (b) absorptance of ordered and random silicon NW arrays from FDTD calculations.

We will first discuss random position and diameter. The xy plane of the simulation domain is an 800 by 800 nm square with periodic boundary conditions, and the z dimension is truncated by the perfectly matched layers. The xy plane is divided into 16 200 by 200 nm cells, and 16 vertical NWs without substrate are used. For random NW position, one NW of 100 nm diameter is placed randomly within each cell. For random NW diameter, the diameter is randomly chosen from 60 to 140 nm and the center of each NW is located at the center of each cell. The NW length is fixed at 2  $\mu\text{m}$ . The structures are shown in Fig. 16. The MIT Electromagnetic Equation Propagation package [38], based on the finite-difference time-domain (FDTD) method, is employed. The silicon dielectric function is adopted from the literature [19]. A spatial resolution  $\Delta x = 10$  nm is chosen and the time step  $\Delta t$  is given by  $0.5\Delta x/c$ , where  $c$  is the speed of light. A source plane, which generates linear-polarized planar waves, is located 1  $\mu\text{m}$  above the NWs. The incident photon frequency is studied in the range of 1.6 to 3.0 eV with a 0.05 eV interval. The reflectance, transmittance, and absorptance at each frequency are calculated using the respective energy flows, as used in our prior work on carbon-nanotube arrays [59]. For each type of randomness, eight distinct configurations are sampled and the results are averaged.

The calculated reflectance data of the ordered and random arrays are shown in Fig. 17(a). The frequency-dependent reflectance of the ordered array is characterized by some oscillations and an evident peak at 2:35 eV. The random-position array shows a similar reflectance profile while the peak slightly shifts to lower frequency. The random-diameter array, in contrast, shows slightly higher reflectance at low frequency and nonoscillating reflectance at higher frequency. The results indicate that frequency dependence is primarily determined by the NW diameters, while their positions only slightly affect the reflectance profile. Also, the reflectances of random position and diameter NW arrays are still quite low and comparable to the ordered array, because forward scattering dominates over backscattering when light strikes on the vertical NW arrays. They differ from those arrays with completely random orientations, where the scattering is nearly isotropic [7], and the reflectance can be as large as 60% [58].

As shown in Fig. 17(b), the absorptance of the ordered array shows a general increase with frequency owing to the increase of the absorption coefficient of silicon. An absorption peak is located at 2.4 eV, which is consistent with the experimental absorption peak of an individual silicon NW with the same diameter reported in[55]. This peak was attributed to the internal resonance. These resonance modes can further induce field enhancement and absorption peaks at certain frequencies. Because of the large aspect ratio of NWs, the resonance frequencies are determined by the diameters but not length. Figure 18(a) shows the energy density on a vertical cross section of a NW under the illumination of two different

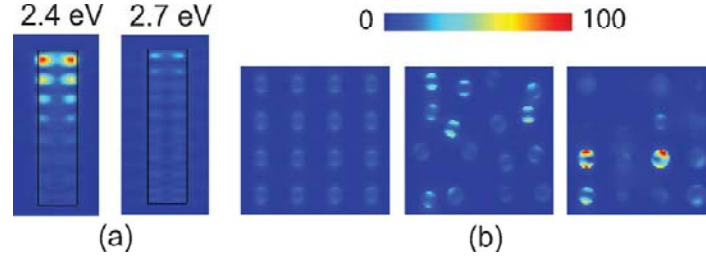


Fig. 18: (a) Energy densities of an individual NW at two different frequencies. (b) Energy density distributions at an xy cross section of ordered, random-position, and random diameter NW array. Single-frequency continuous sources are used to generate the plots. The color bar shows the ratio of the energy density to the incident energy density.

frequencies. Clearly, the 2.4 eV source induces larger field enhancement than the 2.7 eV one. This explains why the NW array has stronger absorption at 2.4 eV than 2.7 eV, even though silicon is more absorptive at the latter frequency. For the random-position NW array, the absorption peak is preserved, because the diameter remains uniform. The overall absorptance is slightly larger than ordered NWs, indicating enhanced multiple scattering and extended optical path length. In the case of a random-diameter array, there is no evident absorption peak, because different diameters give different resonance frequencies as well as absorption peaks. As such, the absorptance is significantly broadened and enhanced for those originally off-resonance frequencies. Interestingly, the absorptance at the original resonance frequency is not deteriorated, although most NWs are no longer at this diameter. This indicates significant enhancement of multiple scattering induced by the random arrangement or diameter, similar to those observed in two-dimensional random media. Although the randomness here is not along the incident direction, the incident wave is diffracted by this subwavelength structure and then multiple scattered. To show the internal resonance and scattering effects more clearly, the energy densities at a horizontal cross section of the three different NW arrays are plotted in Fig. 18(b). In the ordered array, each individual NW has a resonance mode characterized by two lobes (the source is polarized in the y direction). NWs in the random-position array have a similar mode profile, but the electric and magnetic fields are further enhanced because of the enhanced scattering within random media. In the random-diameter array, different NWs have different mode profiles and even stronger field enhancement is seen.

Random lengths can be introduced on purpose to further suppress the reflection. Numerical calculations have shown that less-dense NW arrays have smaller reflection. However, sufficient volume fraction is still needed to effectively absorb light. To overcome this dilemma, modifications of the structures have been proposed, such as the dual-diameter arrays [60] and nanocone array [61], which creates either an intermediate layer with small local volume fraction or a gradually varying volume fraction. Therefore, the dielectric contrast as well as reflection is reduced. Alternatively, we propose to use an NW array with random lengths, which can also generate varying volume fraction, hence reducing reflection. In addition, random length is expected to induce multiple scattering and field localization, analogous to the random textured surface in thin-film solar cells. Such a structure is much simpler than the nanocone and dual-diameter structures. To investigate the effects of random length, we use NWs with ordered position and uniform diameter. Two different sets of diameter are simulated, including 100 and 160 nm, and the corresponding arrays have a volume fraction  $f$  of 0.2 and 0.5, respectively. The lengths are randomly picked from 1 to 2  $\mu\text{m}$  with a uniform probability distribution. The average length is thus 1.5  $\mu\text{m}$ . The lower surfaces of all NWs are kept on the same plane; hence, a rough top surface with a

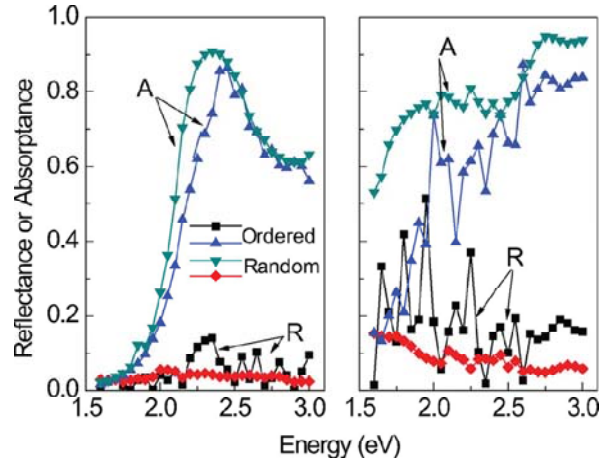


Fig. 19: Reflectance and absorptance of ordered and random-length NW array with volume fraction of 0.2 (left) and 0.5 (right). R denotes reflectance and A denotes absorptance.

roughness of 1  $\mu\text{m}$  is created. The calculated reflectance and absorptance are compared with those of uniform length (1.5  $\mu\text{m}$ ), as shown in Fig. 19. The absorption is significantly enhanced for both volume fractions, and the reflectance does not oscillate with the frequency any more owing to the rough top surface. For the  $f=0.2$  case, the reduction of reflectance is not significant, since it is already quite small, so the enhanced absorption is mostly due to the optical scattering induced by the random top surface. In contrast, the suppression of reflectance is significant for the  $f=0.5$  case.

## 7. Templated SWCNT synthesis in PAA

Some of the earliest studies of nanoscale templating involved porous anodic alumina (PAA)[62, 63]. PAA is formed by anodic oxidation of Al in an acidic electrolyte. The Al is typically either a foil that is several tens of microns thick or a substrate-supported thin-film. The resulting alumina template consists of vertical pores in a naturally occurring hexagonal arrangement[64-68]. The pore diameter is linearly dependent on the anodization electrolyte and voltage—demonstrated pore diameter ranges from sub-10 nm to several hundred nanometers [69, 70]. Advances in electron microscopy amplified the scientific study of PAA [71], and today it is used in a myriad of applications, from a dye-support on the casing of commercial aluminum products (e.g., flashlights, lipstick cases) to a template for supporting the electrochemical formation of nanowires.

The earliest reports of CNTs templated in PAA involve MWCNTs synthesized with or without a deposited catalyst in the pores. When synthesizing MWCNTs in PAA without a catalyst, the main formation mechanism is the adsorption of carbon on the alumina pore walls by the decomposition of hydrocarbons, and this process yields tubes of low crystalline quality [72, 73]. Reported MWCNT synthesis methods utilizing a catalyst include the use of Co [74-76] or Ni [75-77] deposited within the pores followed by MWCNT synthesis. These processes yield MWCNTs that take on the diameter of the pores and typically have a high concentration of disordered carbon but they provide excellent control of the length and diameter of the MWCNTs by varying the dimensions of the PAA.

However, it is typically more difficult to achieve SWCNT synthesis from customized templates or catalysts because of their relatively high activation energy in comparison to MWCNTs [78, 79]. Additionally, nucleation of SWCNTs requires catalyst particles of diameters less than a few nanometers, a size that is not easily achieved when fashioning a catalyst within a template. These two obstacles of high activation energy and difficult catalyst particle size-control are overcome in the present work by burying a Fe catalyst layer in a PAA template and synthesizing in a high temperature microwave plasma-enhanced chemical vapor deposition (MPCVD) environment [80]. The plasma helps to lower the required thermal activation energy by providing a separate means for dissociating the hydrocarbon precursors, thus



relieving part of the energy burden from the catalyst particle. Secondly, covering Fe with a thin layer (few nanometers) of alumina (as is the case on the pore sidewalls of the modified PAA template) raises the surface diffusion barrier of the catalytic Fe particles and thus keeps them from agglomerating [81].

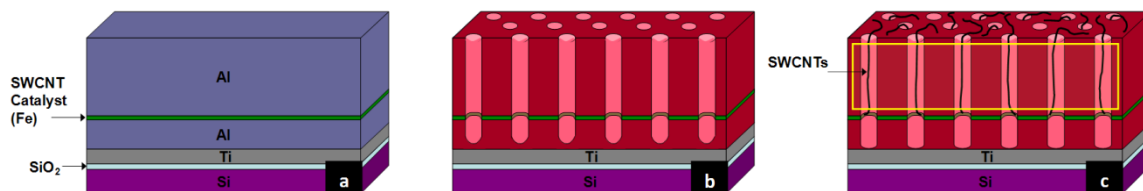


Fig. 20 Cross-sectional schematic of (a) metal film stack deposited on Si wafer, (b) PAA film after anodization, and (c) SWCNTs emerging from PAA pores after undergoing MPCVD synthesis; the box emphasizes the vertical SWCNT channels.

The catalytically active PAA template is formed by first depositing a Ti/Al/Fe/Al film stack on a SiO<sub>2</sub> covered Si wafer, as shown in Figure 20(a). The Ti serves as an adhesion layer for the film and a conductive layer for anodization and other post-processing. Typically, the first (bottom) Al layer is 100 – 200 nm thick, while the top Al is 200 – 1000 nm thick, and the sandwiched Fe layer is approximately 1 nm thick. Anodization is carried out in an acidic electrolyte maintained at 5°C under a constant voltage that is applied with respect to a Pt gauze counter electrode. While there are several electrolytes that can be used in the formation of PAA, 0.3M oxalic acid provides pores of  $\approx 20$  nm diameter at an anodization voltage of 40 V, which is a good average size when working with the present catalytically-active PAA. Larger pores or smaller pores can be obtained by anodizing in phosphoric acid or sulfuric acid, respectively [82].

Anodization of Al takes place by the exchange of Al<sup>3+</sup> anions from the Al film with O<sup>2-</sup> and OH<sup>-</sup> cations from the electrolyte. The exchange of these ions results in two main reactions: 1) the growth of Al<sub>2</sub>O<sub>3</sub> at the Al/Al<sub>2</sub>O<sub>3</sub> interface and 2) the dissolution of Al<sub>2</sub>O<sub>3</sub> at the Al<sub>2</sub>O<sub>3</sub>/electrolyte interface [66]. These reactions result in the formation of alumina pores that proceed perpendicularly from the surface of the Al film. Upon reaching the embedded Fe layer, the anodization current rises by approximately 20 mA as the growth-front of the PAA breaks through the thin Fe layer and continues to grow into the bottom Al layer. In this way, the Fe catalyst becomes embedded in the Al<sub>2</sub>O<sub>3</sub> film, exposing it for catalytic activity at the inner pore sidewalls. Anodization is complete when the current falls below 1 mA, indicating the complete oxidation of the Al and termination of the Al<sub>2</sub>O<sub>3</sub> formation at the Ti layer.

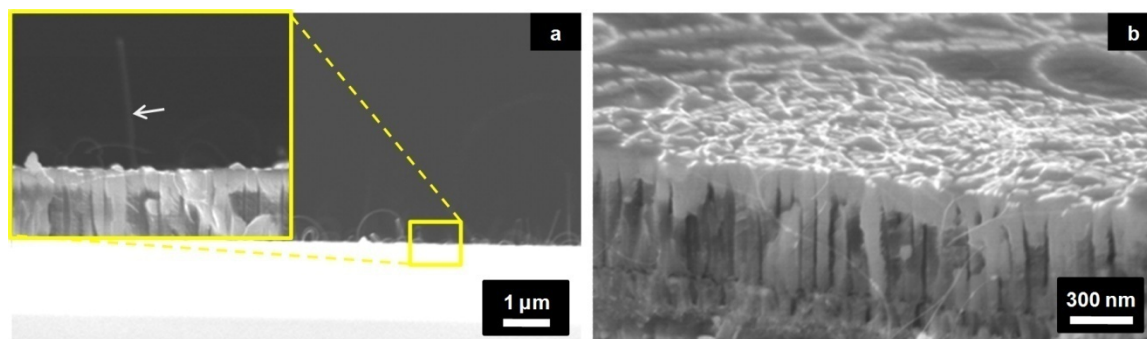


Fig. 21 Cross-sectional SEM images of (a) SWCNTs growing vertically from PAA and (b) SWCNTs draping along the PAA surface and appearing as bright strands.

Synthesis of the SWCNTs from the catalytically active PAA is accomplished in a hydrogen-supported MPCVD with methane as the hydrocarbon precursor gas. Observations to date indicate that only one SWCNT nucleates in any given pore, likely because of the limited gaseous-carbon supply and the

relatively high activation energy required for nucleation. After nucleating at the sidewall of a pore, the SWCNT proceeds to grow vertically to the surface of the PAA, toward the carbon supply. Evidence of this vertical growth is seen in cross-sectional field-emission scanning electron microscope (SEM) images showing freestanding, vertical SWCNTs, as shown in Figure 21(a). However, most SWCNTs grow too long to remain vertical and instead lay horizontally across the PAA surface as seen in Figure 21(b).

In our work, we have also advanced the synthesis approach using nanoimprint lithography (NIL). NIL can solve many of the issues involved in E-beam lithography. In this method, a stamp piece of a stronger material is placed in the electron beam's path. After the development of the photoresist and the subsequent etching away of the unwanted metal, the stamp piece is created. This piece can then be used in the NIL machine itself. Photoresist is spun onto the future sample, and then the future sample and the stamp piece are pressed together in the NIL machine at hundreds of pounds per square inch and temperatures above the melting point of the photoresist. The melted photoresist then viscously flows into the cavities created by the stamp. The temperature drops and the resist hardens, resulting in a mirror image of the stamp piece. This mirror image, the new sample, can then have the unwanted part of the pattern etched away, leading to a cheaply produced and easily reproduced sample, whose only limits are the size of the pattern in the electron beam lithography machine [83].

Chou and others have experimented extensively with NIL since its discovery. Initially able to create sub-25 nm patterns [83], the decreasing size of patterns and increasing ability to manufacture smaller objects has led to recent papers being able to well duplicate sub-5 nm objects [84]. Stamp lifetime and sticking of the photoresist are other areas of interest for research [85]. Obtaining well-ordered PAA was the next step in the NIL process. Creating a stamp out of silicon carbide and pressing it into the aluminum layer can result in near perfect ordered samples [65, 68]. In this method the master stamp of SiC is made by electron-beam lithography and pressed into the PAA, indenting the pore sites in it. The master stamp had negative resist applied to it, so after development and etching pillars would result in the stamp. When it was pressed into the photoresist on top of the eventual PAA sample, small circles which would eventually become pores, and anodization formed the actual PAA. The size of the master was 4 mm x 5 mm, a relatively large area [65]. Using a Cr deposition on a Si substrate, a 3 mm x 3 mm pattern was replicated quite well, indicating that this method of stamp creation has merit as well [85].

The sample is then placed in a Panasonic Reactive Ion Etch (RIE) in order to remove the unwanted silicon. The stamp height is then checked in a profilometer to ensure that the aspect ratio is between the recommended bookends of 3 to 1 to 5 to 1, as in Fig. 22. If it is, the stamp can then be used in the next step.

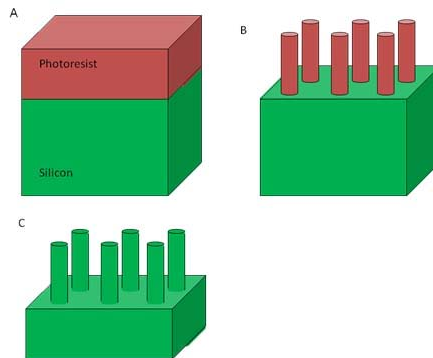


Fig. 22: (A) Silicon piece with photoresist. (B) Silicon piece with patterned and developed photoresist. (C) Silicon piece with pattern etched.

The stamp is then removed, and the pattern is imprinted in the resist left on the sample, as seen in Fig. 23(A). After the NIL stamping, there is a thin layer of resist left in the areas where the stamp was pressing the pieces together, which is easily removed with a short RIE process. This process, a basic 15 sccm oxygen etch at 150 W for 30 seconds to remove photoresist, is short enough that it removes the resist from where it is unwanted while still leaving enough there to protect the parts it is meant to protect.



After this step, we have almost the reverse of our original stamp, which is shown schematically in Fig. 23(B). A second very short RIE process is then used to etch into the top layer of aluminum on our sample that we just stamped into in order to characterize the anodization beginning points. The NXR-1025 can then be removed, leaving an imprinted pattern in the top of the metal stack, as seen in Fig. 23(C).

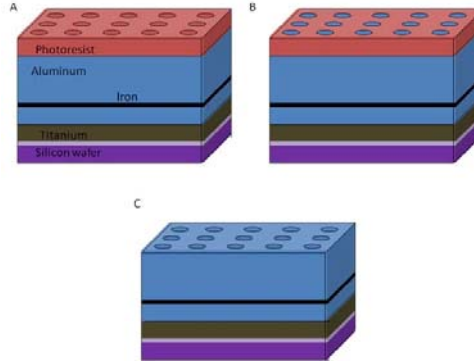


Fig. 23: (A) The metal stack after NIL imprinting. (B) The metal stack after the photoresist etch. (C) The metal stack after the RIE etch and photoresist removal.

After the stamp has been made and used to create the basic pattern in our sample, we must anodize the aluminum to create porous anodic alumina (PAA). After CNT growth, the sample can be coated with 30 nm of alumina by an atomic layer deposition (ALD) machine. The alumina conformally coats the sample, so the film is uniform in thickness and fills the pores while simultaneously coating the

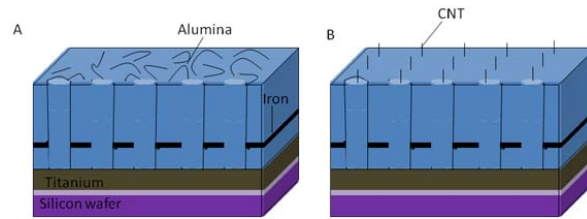


Fig. 24: (A) CNTs in PAA sample after ALD deposition of alumina (B) CNTs in PAA sample after ALD deposition and final etches.

top surface. This results in an alumina sample, 30 nm thicker than before, with the pores filled. The CNTs are still on the surface, but they are coated with the alumina, as seen in figure 24(A). After the ALD process, the film is etched away using the chromic acid for 6 minutes. Most of the CNTs are then etched away using an RIE process of 60 sccm of argon at 1 mtorr for 30 seconds at 300 W of coil power, leaving just tips sticking out of the sample. This results in an alumina sample of the same thickness as the

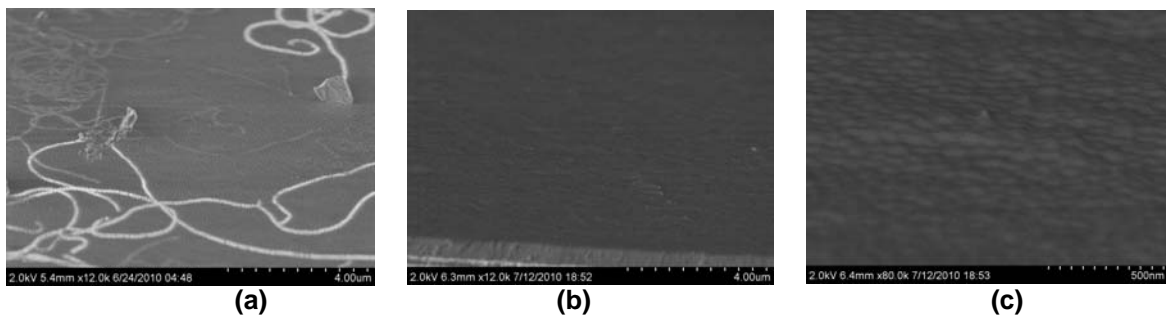


Fig. 25: (a) Top view of PAA sample with CNT growth and alumina coating from an ALD process. (b) an RIE etch to expose CNT tips; (c) the sample after anodization, CNT growth, ALD process of alumina, and final etches to obtain CNT tips.

previous PAA with CNTs sample, only with filled pores and CNT tips, the better to be used in future measurements that call for vertical CNTs and evidenced in Fig. 24(B). As can be seen in Fig. 25, the CNTs on the surface of the sample have disappeared. The RIE process etched away the overhanging CNTs, but the tips remain. However, the reduction to CNT tips has decreased the surface area covered by CNTs. The eventual ideal 1 to 1 CNT to pore growth will help the measurement become more accurate.

## 8. CNT array thermal radiative property characterizations

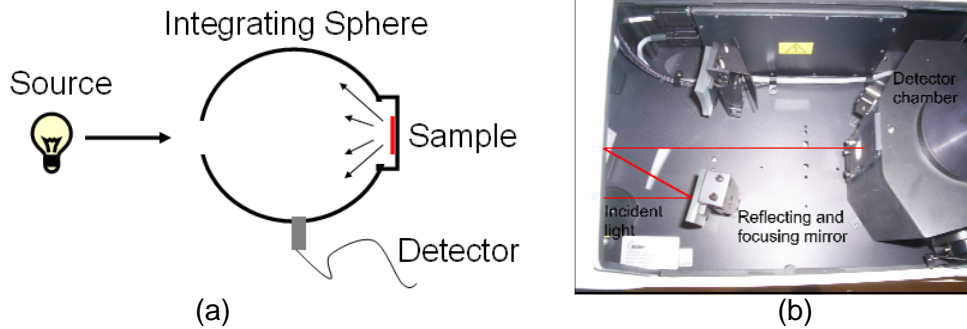


Fig. 26 (a) A sketch of integrating sphere measurement. (b) the actual experimental set-up

The radiative properties of the CNT array samples have been measured by a PerkinElmer Lambda 950 spectrometer with an integrating sphere. The experimental setup is shown in Fig. 26. The integrating sphere reflectance measurement allows for data to be taken over a larger wavelength range and provides a view towards applications with a non focused light source.

The experimental and theoretical reflectance profiles show good agreement with some discrepancies, as seen in Fig. 27. The theory overpredicts reflectance between 250 and 350 nm, and underpredicts it from 350 to 1100 nm. However, the peaks and troughs of the theory and reality are very similar in location, and their difference is most likely due to uncertainties or variations in the thickness of the sample. However, multiple measurements indicate the thickness is 750 nm, and the thickness would not

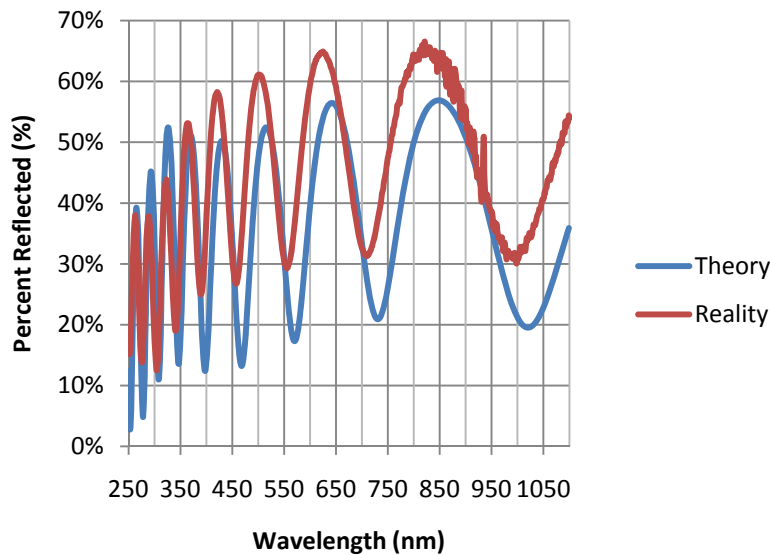


Fig. 27: A comparison between the theoretically calculated reflectance measurement and the actual reflectance measurement for a 750 nm thick PAA sample.

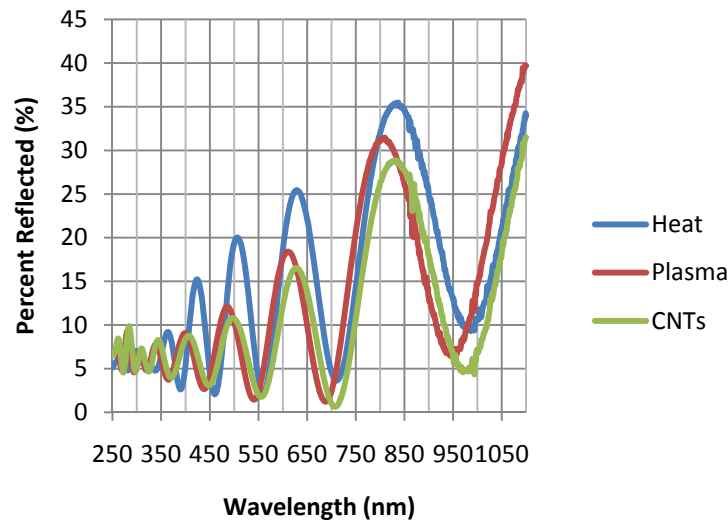


Fig. 28: Reflectance measurements of the three pieces of PAA broken from the same original anodized piece and allowed to complete different parts of the CVD process.

affect the amount reflected as much as it deviates from the theory. Nevertheless, the measurements are relatively in agreement with the theory. Adding in the full metal stack in the calculation may help matters, as would finding a way to add in the pores. The theory used alumina for the model, as reflectance and extinction coefficients for PAA do not exist, and ignored the iron layer in the PAA, assuming it to have a minimal effect, and the silicon and silicon dioxide layers under the titanium, assuming the titanium semi-infinite. The pores probably are what are causing the differences between the theory and measurements, as alumina and PAA are quite different, while the effect of the iron, silicon, and silicon dioxide layers are minimal. Indeed, adding in those layers adds little of value to the theory, proven in Fig. 27, so it is simpler to ignore them.

The different steps of the PECVD process all affect the reflectance measurements of samples. Heating the sample to 900 degrees Celsius, introducing the hydrogen plasma, and introducing the methane all change the reflectance properties of the PAA sample. When the sample is heated to 900 degrees, as seen in figure 28, the reflectance of the sample drops 30 to 40 percent. However, introducing the plasma and the methane do alter the reflectance results. The reflectance peak near 800 nm changes from 807 nm in the PAA piece to 810 nm, and adding methane shifts that peak from 820 nm to 833 nm. In both the plasma and CNT growth graphs, the data in the Ultraviolet (UV) range shifted leftward from where the basic PAA peaks were at. The altered sample data appears to have stretched the results outward.

The plasma also lowers the reflectance another 5-10 percent, and the CNTs that are grown reduce the reflectance another 2-3 percent after that. This results in a total peak reflectance decrease from the MPCVD process of 25% at 287 nm (minimum) to 50% at 500 nm (maximum). Measurements at near infrared (NIR) wavelengths seem to indicate a reduction of 37%. Much of the peak decrease in reflectance comes in the visible range, and the minimum decreases occur at the ultraviolet (UV) wavelengths. However, the UV wavelength peaks are also the most absorbent of all the wavelength peaks. Our theory assumed a semi-infinite titanium layer or a semi-infinite silicon layer underneath the sample, and the extinction coefficients of both silicon and titanium allow this to be an acceptable assumption. Thus, no light is transmitted in our ideal case, resulting in the light being only reflected and absorbed. The less than 10% reflected by the CNTs in the UV range results in 90% absorbed. Even when the NIR measurements are used, over 70% of the incident light is absorbed by the sample, and those are numbers at the peaks. 550 nm and 716 nm in the visible spectrum both have less than 2% reflected,

resulting in over 98% absorbed, while the entire UV spectrum oscillates between 90 and 95% absorbed. If incident light could be focused to these wavelengths, the absorption amounts would be immense.

Measurements of the reflectance of the full process from the PAA sample without CNTs grown to the CNT tips sticking out of the alumina piece were taken after each step: after the PAA construction, after CNT growth, after the ALD process, and after the final etch to expose the CNT tips.

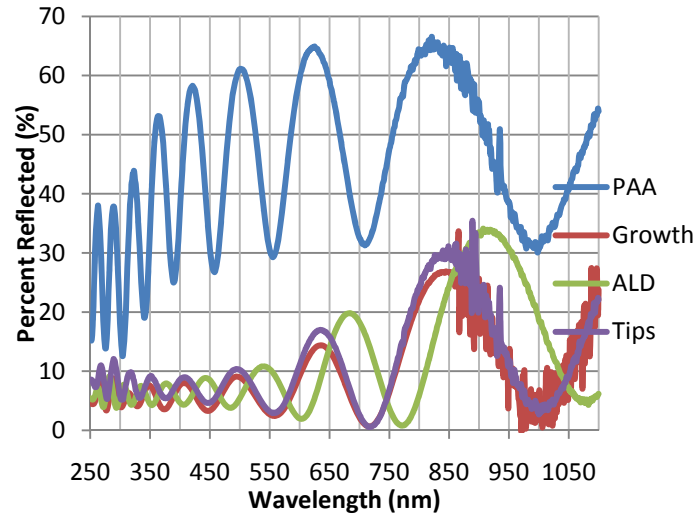


Fig. 29: A diffuse reflectance comparison of the four steps in the process to measure the reflectance of vertical SWCNTs.

For the CNT growth step, +150V bias was added to increase the CNT yield as much as possible. It is worth noting that the 30 nm of ALD alumina added in drastically alter the reflectance and actually increase it in the visible and infrared (IR) spectrum. If we take the theoretical measurements and change the thickness to 780 nm, we see a noticeable phase difference with increases in reflectance at the 510 nm and 635 nm peaks, as seen in Fig. 29. So the rise in reflectance is not to be doubted, especially as many of the CNTs are coated by the alumina and cannot absorb the light. After the chromic etch and RIE, however, the CNT tips return almost exactly to the same wavelengths of reflectance with some small increase in reflectance. The increase in surface area to CNT ratio probably accounts for that, but it is worth noting that above the UV range the vertical CNTs reflect almost identically to CNTs in PAA.

We finally performed the bi-directional reflectance distribution function (BRDF) measurements. The BRDF setup allows for more specific analysis of samples; distinct input angles for the light can be chosen as can exact angles for the detector. That lobe exists for all measurements, be they PAA or the fully etched tips. The graph with CNTs at 35 degrees was chosen because it most clearly shows the pattern. The large spike in the data at the incident angle is a result of the specular light also being measured by the detector. The detector generally measures the diffuse light at the chosen angle, giving the BRDF, but as the difference between incident and detector angle decreases, the specular light enters the detector and greatly increases the number of counts. As for the lobe, the rough PAA surface is a major cause; specular measurements on rough surfaces can cause strong off-specular peaks due to masking and shadowing of the surface from adjacent rough peaks [86]. The rough surface is trapping some of the light in between different facets in the surface, even in the ALD deposited sample. The PAA could have two overlapping crystal vibrational bands, which could cause the lobe. Jasperse et al. [87] found that MgO and LiF crystals had a similar lobe caused by phonon excitation, and Torrance et al. [86] found a way to accurately model the reflectances for rough surfaces. The rough PAA surface could even be causing an antenna effect, which could produce the secondary lobe. However, as radiative effects can depend on impurities and defects that can change between samples, some caution must be taken. All the BRDF

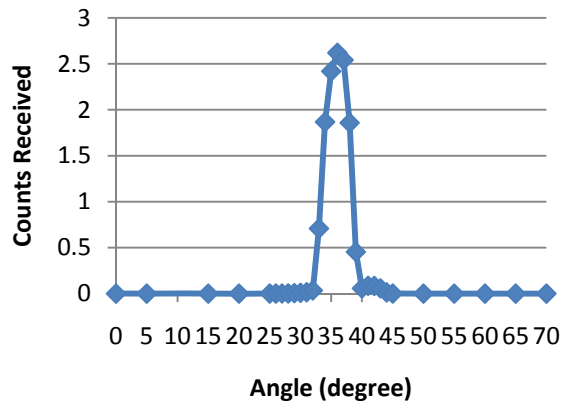


Fig. 30: BRDF measurement at 35 degrees of CNT growth at a 35 degree input angle, illustrated here to indicate the lobe evident on the bottom right half of the parabola.

measurements were done on the same sample. Some general characteristics of the graphs can be attributed. The peak of the reflectance was often not at the same angle as the incident light, but instead one degree more. This could be a result of the system not holding the sample in an equal fashion; the mask used could be slightly displacing the sample. It could also be a consequence of the system's precision. However, with the fact that all measurements indicate an increase in the peak angle relative to incidence, another physical factor may be surmised. In such a case, the results may be an indication of the light hitting the pores in the alumina and reflecting out at a very slightly different degree than expected, giving us the results indicated. The results could have been caused by the CNTs were it not for the one degree alteration evidenced in the pure PAA graph. After the last measurement, however, when the CNTs in pores were replaced by CNT tips positioned in alumina, the peak of the measurements was actually one degree less than the incident angle.

As incident angle increased, the amount of light reflected generally increased, with a few exceptions. The amount of light reflected in the lobe also increased as angle increased. However, 35 degrees and 40 degrees were quite comparable no matter what step in the process. 55 degrees also seems very inconsistent with a lot of the other measurements, but this probably stems from the fact that as incident angle increased, lining up the light source correctly on the sample became more and more difficult. This is yet another reason that measurements were not taken for incident light beyond 55 degrees, as lining up the incident light was much more difficult and prone to error. The Brewster's angle for alumina is approximately 59-60°, depending on which value is used for the reflectance coefficient. Brewster's angle is the angle at which light of one polarization is completely transmitted, and the light reflected is of the opposite polarization. The fact that PAA is slightly different from alumina could lead to a slightly lesser Brewster's angle; that is, since PAA is porous alumina, the pores could be affecting the refractive index and lessening the amount of polarized light that the detector could see reflected back.

## References:

- [1] K. A. Watson, S. Ghose, D. M. Delozier, J. G. Smith, and J. W. Connell, "Transparent, flexible, conductive carbon nanotube coatings for electrostatic charge mitigation," *Polymer*, vol. 46, pp. 2076-2085, 2005.
- [2] T. Trupke, E. Daub, and P. Wurfel, "Absorptivity of silicon solar cells obtained from luminescence," *Solar Energy Materials and Solar Cells*, vol. 53, pp. 103-114, 1998.
- [3] A. Narayanaswamy and G. Chen, "Thermal emission control with one-dimensional metalodielectric photonic crystals," *Phys. Rev. B*, vol. 70, p. 125101, 2004.
- [4] K. Kempa, B. Kimball, J. Ryhczynski, Z. P. Huang, P. F. Wu, D. Steeves, M. Sennett, M. Giersig, D. V. G. L. N. Rao, D. L. Carnahan, D. Z. Wang, J. Y. Lao, W. Z. Li, and Z. F. Ren, "Photonic Crystals Based on Periodic Arrays of Aligned Carbon Nanotubes," *Nano. Letters*, vol. 3, pp. 13-18, 2003.
- [5] V. Yannopapas, "Thermal emission from three-dimensional arrays of gold nanoparticles," *Phys. Rev. B*, vol. 73, p. 113108, 2006.
- [6] G. Torsello, M. Lomascolo, A. Licciulli, D. Diso, S. Tundo, and M. Mazzer, "The origin of highly efficient selective emission in rare-earth oxides for thermophotovoltaic applications," *Nat. Mater.*, vol. 3, p. 632, 2004.
- [7] Z. M. Zhang, *Nano/Microscale Heat Transfer*. New York: McGraw-Hill, 2007.
- [8] R. M. Martin, *Electronic Structure: Basic Theory and Practical Methods*. Cambridge, UK: Cambridge University Press, 2004.
- [9] G. Y. Guo, K. C. Chu, D. S. Wang, and C. G. Duan, "Linear and Nonlinear Optical Properties of Carbon Nanotubes from First-principles Calculations," *Phys. Rev. B*, vol. 69, p. 205416, 2004.
- [10] X. Gonze and C. Lee, "Dynamical matrices, Born effective charges, dielectric permittivity tensors, and interatomic force constants from density-functional perturbation theory," *Phys. Rev. B*, vol. 55, p. 10355, 1997.
- [11] K. Lee and W. E. Pickett, "Born effective charges and infrared response of  $\text{LiBC}$ ," *Phys. Rev. B*, vol. 68, 2003.
- [12] X. Gonze, J.-M. Beuken, R. Caracas, F. Detraux, M. Fuchs, G.-M. Rignanese, L. Sindic, M. Verstraete, G. Zerah, F. Jollet, M. Torrent, A. Roy, M. Mikami, P. Ghosez, J.-Y. Raty, and D. C. Allan, "First-principles computation of material properties : the ABINIT software project," *Comput. Mater. Sci.*, vol. 25, pp. 478-492, 2002.
- [13] N. Troullier and J. L. Martins, "Efficient pseudopotentials for plane-wave calculations," *Phys. Rev. B*, vol. 43, pp. 1993-2006, 1991.
- [14] V. Fiorentini, "Semiconductor band structures at zero pressure," *Phys. Rev. B*, vol. 46, p. 2086, 1992.
- [15] M.-Z. Huang and W. Y. Ching, "A Minimal Basis Semi-*ab initio* Approach to the Band Structures of Semiconductors," *J. Phys. Chem. Solids*, vol. 46, pp. 977-995, 1985.
- [16] C. Kittel, *Introduction to Solid State Physics*. New York: John Wiley, 1996.
- [17] H. Ehrenreich, H. R. Philipp, and J. C. Phillips, "Interband Transitions in Groups 4, 3-5, and 2-6 Semiconductors," *Phys. Rev. Lett.*, vol. 8, pp. 59-61, 1962.
- [18] M.-Z. Huang and W. Y. Ching, "Calculation of optical excitations in cubic semiconductors. I. Electronic structure and linear response," *Phys. Rev. B*, vol. 47, p. 9449, 1993.
- [19] E. D. Palik, *Handbook of Optical Constants of Solids*: Elsevier, 1998.
- [20] D. L. Rousseau, R. P. Bauman, and S. P. S. Porto, "Normal mode determination in crystals," *J. Raman Spectrosc.*, vol. 10, p. 253, 1981.
- [21] J. S. Blakemore, "Semiconducting and other Major Properties of Gallium Arsenide," *J. Appl. Phys.*, vol. 53, pp. R123-R181, 1982.
- [22] Y. S. Touloukian and D. P. DeWitt, *Thermophysical Properties of Matter*. New York: IFI Plenum, 1970-1972.

- [23] N. Troullier and J. L. Martins, "Efficient Pseudopotentials for Plane-Wave Calculations," *Physical Review B*, vol. 43, pp. 1993-2006, Jan 15 1991.
- [24] E. R. Davidson, "Iterative Calculation of a Few of Lowest Eigenvalues and Corresponding Eigenvectors of Large Real-Symmetric Matrices," *Journal of Computational Physics*, vol. 17, pp. 87-94, 1975.
- [25] S. Ismail-Beigi, "Truncation of periodic image interactions for confined systems," *Physical Review B*, vol. 73, pp. -, Jun 2006.
- [26] M. J. O'Connell, S. M. Bachilo, C. B. Huffman, V. C. Moore, M. S. Strano, E. H. Haroz, K. L. Rialon, P. J. Boul, W. H. Noon, C. Kittrell, J. P. Ma, R. H. Hauge, R. B. Weisman, and R. E. Smalley, "Band gap fluorescence from individual single-walled carbon nanotubes," *Science*, vol. 297, pp. 593-596, Jul 26 2002.
- [27] J. Deslippe, C. D. Spataru, D. Prendergast, and S. G. Louie, "Bound excitons in metallic single-walled carbon nanotubes," *Nano Letters*, vol. 7, pp. 1626-1630, Jun 2007.
- [28] C. Fantini, A. Jorio, M. Souza, M. S. Strano, M. S. Dresselhaus, and M. A. Pimenta, "Optical transition energies for carbon nanotubes from resonant Raman spectroscopy: Environment and temperature effects," *Physical Review Letters*, vol. 93, pp. -, Oct 1 2004.
- [29] Y. Murakami, E. Einarsson, T. Edamura, and S. Maruyama, "Polarization dependence of the optical absorption of single-walled carbon nanotubes," *Physical Review Letters*, vol. 94, pp. -, Mar 4 2005.
- [30] H. Ajiki and T. Ando, "Aharonov-Bohm Effect in Carbon Nanotubes," *Physica B*, vol. 201, pp. 349-352, Jul-Aug 1994.
- [31] B. Kozinsky and N. Marzari, "Static dielectric properties of carbon nanotubes from first principles," *Physical Review Letters*, vol. 96, pp. -, Apr 28 2006.
- [32] M. Y. Koledintseva, R. E. Dubroff, and R. W. Schwartz, "A Maxwell Garnett model for dielectric mixtures containing conducting particles at optical frequencies," *Progress in Electromagnetics Research-Pier*, vol. 63, pp. 223-242, 2006.
- [33] M. Y. Koledintseva, J. Wu, J. M. Zhang, J. L. Drewniak, and K. N. Rozanov, "Representation of permittivity for multiphase dielectric mixtures in FDTD modeling," *2004 International Symposium on Electromagnetic Compatibility, Symposium Record 1-3*, pp. 309-314 1038, 2004.
- [34] Y. M. Li, D. Mann, M. Rolandi, W. Kim, A. Ural, S. Hung, A. Javey, J. Cao, D. W. Wang, E. Yenilmez, Q. Wang, J. F. Gibbons, Y. Nishi, and H. J. Dai, "Preferential growth of semiconducting single-walled carbon nanotubes by a plasma enhanced CVD method," *Nano Letters*, vol. 4, pp. 317-321, Feb 2004.
- [35] K. Mizuno, J. Ishii, H. Kishida, Y. Hayamizu, S. Yasuda, D. N. Futaba, M. Yumura, and K. Hata, "A black body absorber from vertically aligned single-walled carbon nanotubes," *Proceedings of the National Academy of Sciences of the United States of America*, vol. 106, pp. 6044-6047, Apr 14 2009.
- [36] L. Henrard and P. Lambin, "Calculation of energy loss for an electron passing near giant fullerenes," *J. Phys. B*, vol. 29, p. 5127, 1996.
- [37] L. G. Johnson and G. Dresselhaus, "Optical Properties of Graphite," *Phys. Rev. B*, vol. 7, p. 2275, 1973.
- [38] A. Farjadpour, D. Roundy, A. Rodriguez, M. Ibanescu, P. Bermel, J. D. Joannopoulos, S. G. Johnson, and G. Burr, "Improving accuracy by subpixel smoothing in FDTD," *Opt. Lett.*, vol. 31, pp. 2972-2974, 2006.
- [39] F. J. Garcia-Vidal, J. M. Pitarke, and J. B. Pendry, "Effective Medium Theory of the Optical Properties of Aligned Carbon Nanotubes," *Phys. Rev. Lett.*, vol. 78, pp. 4289-4292, 1997.
- [40] X. L. Ruan and M. Kaviani, "Photon Localization and Electromagnetic Field Enhancement in Laser Irradiated, Random Porous Media," *Microscale Thermophysical Engineering*, vol. 9, pp. 63-84, 2005.



- [41] L. Hu and G. Chen, "Analysis of Optical Absorption in Silicon Nanowire Arrays for Photovoltaic Applications," *Nano Lett.*, vol. 7, pp. 3249-3252, 2007.
- [42] G. L. Zhao, D. Bagayoko, and L. Yang, "Optical properties of aligned carbon nanotube mats for photonic applications," *Journal of Applied Physics*, vol. 99, pp. -, Jun 1 2006.
- [43] W. Z. Li, S. S. Xie, L. X. Qian, B. H. Chang, B. S. Zou, W. Y. Zhou, R. A. Zhao, and G. Wang, "Large-scale synthesis of aligned carbon nanotubes," *Science*, vol. 274, pp. 1701-1703, Dec 6 1996.
- [44] G. Y. Zhang, D. Mann, L. Zhang, A. Javey, Y. M. Li, E. Yenilmez, Q. Wang, J. P. McVittie, Y. Nishi, J. Gibbons, and H. J. Dai, "Ultra-high-yield growth of vertical single-walled carbon nanotubes: Hidden roles of hydrogen and oxygen," *Proceedings of the National Academy of Sciences of the United States of America*, vol. 102, pp. 16141-16145, Nov 8 2005.
- [45] S. S. Fan, M. G. Chapline, N. R. Franklin, T. W. Tombler, A. M. Cassell, and H. J. Dai, "Self-oriented regular arrays of carbon nanotubes and their field emission properties," *Science*, vol. 283, pp. 512-514, Jan 22 1999.
- [46] H. Bao, X. L. Ruan, and T. S. Fisher, "Optical properties of ordered vertical arrays of multi-walled carbon nanotubes from FDTD simulations," *Optics Express*, vol. 18, pp. 6347-6359, Mar 15 2010.
- [47] H. Bao and X. L. Ruan, "Optical absorption enhancement in disordered vertical silicon nanowire arrays for photovoltaic applications," *Optics Letters*, vol. 35, pp. 3378-3380, Oct 15 2010.
- [48] F. J. Garcia-Vidal, J. M. Pitarke, and J. B. Pendry, "Effective medium theory of the optical properties of aligned carbon nanotubes," *Physical Review Letters*, vol. 78, pp. 4289-4292, Jun 2 1997.
- [49] W. G. Lu, J. M. Dong, and Z. Y. Li, "Optical properties of aligned carbon nanotube systems studied by the effective-medium approximation method," *Physical Review B*, vol. 63, pp. -, Jan 15 2001.
- [50] A. Taflove and S. C. Hagness, *Computational electrodynamics : the finite-difference time-domain method*, 3rd ed. Boston: Artech House, 2005.
- [51] J. Zhu, Z. F. Yu, G. F. Burkhard, C. M. Hsu, S. T. Connor, Y. Q. Xu, Q. Wang, M. McGehee, S. H. Fan, and Y. Cui, "Optical Absorption Enhancement in Amorphous Silicon Nanowire and Nanocone Arrays," *Nano Letters*, vol. 9, pp. 279-282, Jan 2009.
- [52] Y. P. Dan, K. Seo, K. Takei, J. H. Meza, A. Javey, and K. B. Crozier, "Dramatic Reduction of Surface Recombination by in Situ Surface Passivation of Silicon Nanowires," *Nano Letters*, vol. 11, pp. 2527-2532, Jun 2011.
- [53] L. Tsakalakos, J. Balch, J. Fronheiser, B. A. Korevaar, O. Sulima, and J. Rand, "Silicon nanowire solar cells," *Appl. Phys. Lett.*, vol. 91, p. 233117, 2007.
- [54] B. Tian, X. Zheng, T. J. Kempa, Y. Fang, N. Yu, G. Yu, J. Huang, and C. M. Lieber, "Coaxial silicon nanowires as solar cells and nanoelectronic power sources," *Nature*, vol. 229, pp. 885-889, 2007.
- [55] L. Y. Cao, J. S. White, J. S. Park, J. A. Schuller, B. M. Clemens, and M. L. Brongersma, "Engineering light absorption in semiconductor nanowire devices," *Nat. Mater.*, vol. 8, pp. 643-647, 2009.
- [56] C. Lin and M. L. Povinelli, "Optical absorption enhancement in silicon nanowire arrays with a large lattice constant for photovoltaic applications," *Opt. Express*, vol. 17, p. 19371, 2009.
- [57] O. L. Muskens, J. G. Rivas, R. E. Algra, E. P. A. M. Bakkers, and A. Lagendijk, "Design of light scattering in nanowire materials for photovoltaic applications," *Nano Letters*, vol. 8, pp. 2638-2642, Sep 2008.
- [58] R. A. Street, P. Qi, R. Lujan, and W. S. Wong, "Reflectivity of disordered silicon nanowires," *Appl. Phys. Lett.*, vol. 93, p. 163109, 2008.
- [59] H. Bao, X. L. Ruan, and T. S. Fisher, "Optical properties of ordered vertical arrays of multi-walled carbon nanotubes from FDTD simulations," *Opt. Express*, vol. 18, pp. 6347-6359, 2010.



- [60] Z. Fan, H. Razavi, J. Do, A. Moriwaki, O. Ergen, Y. Chueh, P. W. Leu, J. C. Ho, T. Takahashi, L. A. Reichertz, S. Neale, K. Yu, M. Wu, J. W. Ager, and A. Javey, "Three-dimensional nanopillar-array photovoltaics on low-cost and flexible substrates," *Nat. Mater.*, vol. 8, pp. 648-653, 2009.
- [61] J. Zhu, Z. Yu, G. F. Burkhard, C. M. Hsu, S. T. Connor, Y. Xu, Q. Wang, M. McGehee, S. Fan, and Y. Cui, "Optical Absorption Enhancement in Amorphous Silicon Nanowire and Nanocone Arrays," *Nano Lett.*, vol. 9, pp. 279-282, 2009.
- [62] J. D. Edwards and T. Keller, "The structure of anodic oxide coatings," *Transactions of the American Institute of Mining and Metallurgical Engineers*, vol. 156, pp. 288-299, 1944.
- [63] F. Keller, M. S. Hunter, and D. L. Robinson, "Structural Features of Oxide Coatings on Aluminium," *Journal of the Electrochemical Society*, vol. 100, pp. 411-419, 1953.
- [64] H. Masuda, F. Hasegawa, and S. Ono, "Self-ordering of cell arrangement of anodic porous alumina formed in sulfuric acid solution," *Journal of the Electrochemical Society*, vol. 144, pp. L127-L130, May 1997.
- [65] H. Masuda, H. Yamada, M. Satoh, H. Asoh, M. Nakao, and T. Tamamura, "Highly ordered nanochannel-array architecture in anodic alumina," *Applied Physics Letters*, vol. 71, pp. 2770-2772, Nov 10 1997.
- [66] O. Jessensky, F. Muller, and U. Gosele, "Self-organized formation of hexagonal pore arrays in anodic alumina," *Applied Physics Letters*, vol. 72, pp. 1173-1175, Mar 1998.
- [67] Z. J. Sun and H. K. Kim, "Growth of ordered, single-domain, alumina nanopore arrays with holographically patterned aluminum films," *Applied Physics Letters*, vol. 81, pp. 3458-3460, Oct 28 2002.
- [68] H. Asoh, K. Nishio, M. Nakao, A. Yokoo, T. Tamamura, and H. Masuda, "Fabrication of ideally ordered anodic porous alumina with 63 nm hole periodicity using sulfuric acid," *Journal of Vacuum Science & Technology B*, vol. 19, pp. 569-572, Mar-Apr 2001.
- [69] A. P. Li, F. Muller, A. Birner, K. Nielsch, and U. Gosele, "Hexagonal pore arrays with a 50-420 nm interpore distance formed by self-organization in anodic alumina," *Journal of Applied Physics*, vol. 84, pp. 6023-6026, Dec 1 1998.
- [70] E. C. Walter, K. Ng, M. P. Zach, R. M. Penner, and F. Favier, "Electronic devices from electrodeposited metal nanowires," *Microelectronic Engineering*, vol. 61-2, pp. 555-561, Jul 2002.
- [71] Osullivan.Jp and G. C. Wood, "Morphology and Mechanism of Formation of Porous Anodic Films on Aluminium," *Proceedings of the Royal Society of London Series a-Mathematical and Physical Sciences*, vol. 317, pp. 511-&, 1970.
- [72] S. H. Jeong, H. Y. Hwang, S. K. Hwang, and K. H. Lee, "Carbon nanotubes based on anodic aluminum oxide nano-template," *Carbon*, vol. 42, pp. 2073-2080, 2004.
- [73] H. Y. Jung, J. Kim, J. Hahn, and J. S. Suh, "Well-ordered semiconducting linearly joined carbon nanotube devices at room temperature," *Chemical Physics Letters*, vol. 402, pp. 535-538, Feb 4 2005.
- [74] P. L. Chen, J. K. Chang, C. T. Kuo, and F. M. Pan, "Anodic aluminum oxide template assisted growth of vertically aligned carbon nanotube arrays by ECR-CVD," *Diamond and Related Materials*, vol. 13, pp. 1949-1953, Nov-Dec 2004.
- [75] M. J. Kim, T. Y. Lee, J. H. Choi, J. B. Park, J. S. Lee, S. K. Kim, J. B. Yoo, and C. Y. Park, "Growth of carbon nanotubes with anodic aluminum oxide formed on the catalytic metal-coated Si substrate," *Diamond and Related Materials*, vol. 12, pp. 870-873, Mar-Jul 2003.
- [76] J. S. Lee and J. S. Suh, "Uniform field emission from aligned carbon nanotubes prepared by CO disproportionation," *Journal of Applied Physics*, vol. 92, pp. 7519-7522, Dec 15 2002.
- [77] J. H. Yen, I. C. Leu, M. T. Wu, C. C. Lin, and M. H. Hon, "Density control for carbon nanotube arrays synthesized by ICP-CVD using AAO/Si as a nanotemplate," *Electrochemical and Solid State Letters*, vol. 7, pp. H29-H31, 2004.

- [78] M. R. Maschmann, A. D. Franklin, T. D. Sands, and T. S. Fisher, "Optimization of carbon nanotube synthesis from porous anodic Al-Fe-Al templates," *Carbon*, vol. 45, pp. 2290-2296, Oct 2007.
- [79] S. Hofmann, G. Csanyi, A. C. Ferrari, M. C. Payne, and J. Robertson, "Surface diffusion: The low activation energy path for nanotube growth," *Physical Review Letters*, vol. 95, pp. -, Jul 15 2005.
- [80] M. R. Maschmann, A. D. Franklin, P. B. Amama, D. N. Zakharov, E. A. Stach, T. D. Sands, and T. S. Fisher, "Vertical single- and double-walled carbon nanotubes grown from modified porous anodic alumina templates," *Nanotechnology*, vol. 17, pp. 3925-3929, Aug 14 2006.
- [81] G. F. Zhong, T. Iwasaki, K. Honda, Y. Furukawa, I. Ohdomari, and H. Kawarada, "Very high yield growth of vertically aligned single-walled carbon nanotubes by point-arc microwave plasma CVD," *Chemical Vapor Deposition*, vol. 11, pp. 127-130, Mar 2005.
- [82] S. Fournier-Bidoz, V. Kitaev, D. Routkevitch, I. Manners, and G. A. Ozin, "Highly ordered nanosphere imprinted nanochannel alumina (NINA)," *Advanced Materials*, vol. 16, pp. 2193-+, Dec 27 2004.
- [83] S. Y. Chou, P. R. Krauss, and P. J. Renstrom, "Imprint of Sub-25 Nm Vias and Trenches in Polymers," *Applied Physics Letters*, vol. 67, pp. 3114-3116, Nov 20 1995.
- [84] M. D. Austin, H. X. Ge, W. Wu, M. T. Li, Z. N. Yu, D. Wasserman, S. A. Lyon, and S. Y. Chou, "Fabrication of 5 nm linewidth and 14 nm pitch features by nanoimprint lithography," *Applied Physics Letters*, vol. 84, pp. 5299-5301, Jun 28 2004.
- [85] S. Zankovych, T. Hoffmann, J. Seekamp, J. U. Bruch, and C. M. S. Torres, "Nanoimprint lithography: challenges and prospects," *Nanotechnology*, vol. 12, pp. 91-95, Jun 2001.
- [86] K. E. Torrance and E. M. Sparrow, "Theory for Off-Specular Reflection from Roughened Surfaces," *Journal of the Optical Society of America*, vol. 57, pp. 1105-&, 1967.
- [87] J. R. Jasperse, A. Kahan, J. N. Plendl, and S. S. Mitra, "Temperature Dependence of Infrared Dispersion in Ionic Crystals Lif and Mgo," *Physical Review*, vol. 146, pp. 526-&, 1966.